GLB-3: a resilient, cysteine-rich, membrane-tethered globin expressed in the reproductive and nervous system of *Caenorhabditis elegans*

Zainab Hafideddine[1,2], Tim Loier[3], Niels Van Brempt[2], Sasha De Henau[3], H. Y. Vincent Ching[2,4], Sander Neukermans[4], Saskia Defossé[2], Herald Berghmans[1], Roberta Sgammato[2], Roy Aerts[2], Dietmar Hammerschmid[2,a], Rani Moons[2], Tom Breugelmans,[4] Frank Sobott[2,b], Christian Johannessen[2], Wouter Herrebout[2], Bart P. Braeckman[3], Luc Moens[1], Sylvia Dewilde[1,†], Sabine Van Doorslaer[2,*]

[1]Department of Biomedical Sciences, University of Antwerp, 2610 Antwerp, Belgium

[2]Departement of Chemistry, University of Antwerp, 2610 Antwerp, Belgium

[3]Department of Biology, Ghent University, 9000 Gent, Belgium

[4]Department of Applied Engineering, University of Antwerp, 2610 Antwerp, Belgium

[a]Current address: Department of Chemistry, King's College London, Britannia House, 7 Trinity Street, London SE1 1DB, United Kingdom

[b]Current address: Astbury Centre for Structural Molecular Biology and the School of Molecular and Cellular Biology, University of Leeds, Leeds LS2 9JT, United Kingdom

[†]passed away on 3rd October 2020

*corresponding author: Sabine Van Doorslaer, BIMEF, Departement of Chemistry, University of Antwerp, Universiteitsplein 1, 2610 Antwerp, Belgium, Phone: +32 3 265 24 61 ; ORCID: https://orcid.org/0000-0002-1685-9202 ; E-mail: sabine.vandoorslaer@uantwerpen.be

Dedication: This work is dedicated to the memory of our dear co-worker, Prof. dr. Sylvia Dewilde, who passed away at the age of 47 during work that led to this paper

Keywords: Globins, spectroscopy, electron paramagnetic resonance (EPR), redox signaling, heme, *Caenorhabditis elegans*

ABSTRACT: The popular genetic model organism *Caenorhabditis elegans* (*C. elegans*) encodes 34 globins, whereby the few that are well-characterized show divergent properties besides the typical oxygen carrier function. Here, we present a biophysical characterization and expression analysis of *C. elegans* globin-3 (GLB-3). GLB-3 is predicted to exist in two isoforms and is expressed in the reproductive and nervous system. Knockout of this globin causes a 99 % reduction in fertility and reduced motility. Spectroscopic analysis reveals that GLB-3 exists as a bis-histidyl-ligated low-spin form in both the ferrous and ferric heme form. A function in binding of diatomic gases is excluded on the basis of the slow CO-binding kinetics. Unlike other globins, GLB-3 is also not capable of reacting with H_2O_2, H_2S, and nitrite. Intriguingly, not only does GLB-3 contain a high number of cysteine residues, it is also highly stable under harsh conditions (pH = 2 and high concentrations of H_2O_2). The resilience diminishes when the N- and C-terminal extensions are removed. Redox potentiometric measurements reveal a slightly positive redox potential (+8 ± 19 mV vs. SHE), suggesting that the heme iron may be able to oxidize cysteines. Electron paramagnetic resonance shows that formation of an intramolecular disulphide bridge, involving Cys70, affects the heme-pocket region. The results suggest an involvement of the globin in (cysteine) redox chemistry.

INTRODUCTION

Globins are α-helical heme-containing proteins that occur as three families: the myoglobin-like (M), the sensor (S), and the truncated (T) family. The heme iron in vertebrate hemoglobin (Hb) and myoglobin (Mb) is coordinated to the conserved His at position 8 of the F helix (F8His), while the opposite coordination site allows the binding of exogenous (diatomic) ligands [1]. In other globins, such as neuroglobin (Ngb), the endogenous E7His is bound to the heme iron (bis-histidine coordination). Exogenous ligands, such as O_2, CO and NO, can then still bind to the heme iron but compete with the distal histidine residue.

For a long time, O_2 binding was thought to be the hallmark feature of globins [2,3]. However, knowledge about the globin superfamily has expanded enormously over the years, revealing globins in all kingdoms of life with a diverse functional repertoire, including O_2 transport and storage function, involvement in NO metabolism, sulfide transport, detoxification of reactive oxygen (ROS) and nitrogen (RNS) species, sensing, and signalling functions [4]. Mb, for instance, not only acts as an NO scavenger, converting NO to NO_3^-, but also as a nitrite reductase to convert NO_2^- to NO in response to NO homeostasis. Peroxidase activity is observed both in Mb and Hb, which could serve to neutralize the ROS-generating H_2O_2 during oxidative stress [5]. Moreover, Hb and Mb also show H_2S oxidizing activity to remove toxic H_2S in blood and heart, respectively [6]. Although it is by now clear that globins are involved in various cellular processes, the exact functions of many globins are still unknown.

In silico analysis of the genome of the small nematode *Caenorhabditis elegans* (*C. elegans*) revealed the presence of 34 globin-like genes with a diversity in sequence, length and intron position [6-10]. The 34 globin genes, encoded as *glb-1* to *glb-34*, are all transcribed and predominantly expressed in specific subsets of neurons, indicative of a signalling function. Currently, only seven *C. elegans* globins are characterized to some extent (Table 1), exhibiting a

variety of functions with several participating in redox reactions [11]. The role of the remaining 27 globins is still completely unknown. A few *C. elegans* globins are proposed to be membrane bound since they are myristoylated and/or palmitoylated (Table 1). One such example, GLB-12, was shown to be anchored to the plasma membrane in the neurons and somatic gonad [11]. Although membrane association of globins has been reported in other species [12-15], it is still a poorly defined attribute of globins.

Here, we characterize *C. elegans* globin GLB-3 using a multitude of techniques. GLB-3 is predicted to exist in two isoforms: GLB-3a and GLB-3b, whereby the a-isoform is an N-terminal truncation of the complete b-isoform. *In vivo* localization shows that GLB-3 is expressed in a set of neurons as well as the somatic gonad. We studied the expression pattern and the mutant phenotypes to characterize GLB-3 function *in vivo*.

In addition, different biochemical and spectroscopic methods were used to gain *in vitro* information on the stability, multimerization, heme iron ligation and spin state, binding kinetics and redox potential of the protein. GLB-3 contains a remarkably high number of cysteine residues (9 in GLB-3a and 12 in GLB-3b). To study the impact of the cysteine residues on the GLB-3 globin structure and function *in vitro*, we analyzed the protein in the absence and presence of the reducing agent DTT. The data indicate that both GLB-3 isoforms are most likely participating in redox reactions rather than exhibiting ligand-binding functions.

Table 1. Summary of the currently known *C. elegans* globin characteristics. The heme coordination is given in the ferric form of the *C. elegans* globins.[a)]

	Localisation	**Heme coord. + Axial ligands**	**Function**	**Myristoy-lation site**	**Palmitoy-lation site**	**Ref.**
GLB-1	Muscle and neuronal	6C/HS His–H_2O	Mb-like, high O_2 affinity		…ISDL**C**VKS L…	[16]
GLB-3	Neuronal, somatic gonad	6C/LS His–His	Redox sensor/e^- transfer	M**G**NDHSV…[b)]	…MNEK**CC** GVVF…	This work
GLB-5	Neuronal	6C/LS His–His	O_2 sensor; modulates feeding response			[17, 18]
GLB-6	Neuronal	6C/LS His–His	Redox sensor/e^- transfer; response to oxidative stress	M**G**NQSTK…		[19]
GLB-12	Neuronal, vulva cells and somatic gonad	6C/LS His–His	Production of O_2^-; influence reproductive system	M**G**ATLCAPK K…	MGATL**C**AP …	[11]
GLB-13	Neuronal	6C	Ngb-like neuroprotective function	M**G**QENSKCP …	MGQENSK**C** PH…	[20]
GLB-26	Muscle, head mesodermal cells	6C/LS His–His	e^- transfer; regulation of defecation cycle	M**G**SSTSTP…		[21, 22]
GLB-33	Neuronal	6C/LS His–OH	Neuropeptide receptor (GD-7TM) with high O_2 affinity and nitrite reductase activity		…YVSL**C**AL LF…	[23]

[a)] N-terminal myristoylation is also predicted for the *C. elegans* GLB-11, GLB-17 and GLB-20 with a high confidence level. S-palmitoylation is also anticipated in *C. elegans* GLB-17, GLB-21 and GLB-29; [b)] only predicted for GLB-3b isoform.

1. MATERIALS AND METHODS

1.1. General methods and strains

The *C. elegans* strains used for the phenotyping experiments were obtained from the CGC: N2 Bristol WT and VC2879 [*glb-3(ok3630) V/nT1 [qIs51]* (IV;V)]. Since *glb-3* knockout causes sterility, the VC2879 strain is balanced for the deletion by GFP-marked translocation. Heterozygotes are marked with a pharyngeal GFP signal, while homozygous *nT1[qIs51]* are inviable. *glb-3* homozygotes are mostly sterile and possess no GFP signal. These were manually picked from the population for all phenotyping experiments. For strain maintenance, GFP heterozygotes were picked and checked for correct segregation. Worms were, in general, maintained according to standard procedures [24], but cultured at 16 °C on nutrient agar seeded with a lawn of *Escherichia coli* K12 [25]. For experiments, worms were synchronized according to standard bleaching procedures [26]. Eggs were allowed to hatch overnight in S buffer (0.1 M NaCl, 50 mM potassium phosphate buffer at pH 6) and subsequently plated on nutrient agar plates containing *Escherichia coli* OP50. Experimental plates were kept at 20 °C.

2.2. *glb-3* imaging

The *glb-3* translational reporter was made using fusion PCR [27]. The reporter contains both isoforms of the *glb-3* gene and includes the endogenous promoter and 3′UTR elements. The *gfp* gene was amplified from the vector pPD95.75 (Fire Lab) and fused at the 3′ side of the *glb-3* coding gene and preceding the *glb-3* 3′UTR region. The primers that were used are 5’-CAT-CGC-GCG-CAC-CGT-ACG-TCG-AAC-TGT-CTA-TTT-GGC-TGA-C-3’ and 5’-CCA-GCG-CCT-GCA-CCA-GCT-CCT-GCA-TAT-GGA-CCT-GAA-AAC-3’ to amplify the *glb-3* promoter and gene region, and 5’-CTC-ATC-ACC-ATC-ACC-ATC-ACT-AAA-ATC-AGG-TCA-TCT-ATC-ATC-A-3’ and 5’-ACG-TAA-TAC-GAC-TCA-CTT-AAA-TCG-CCG-CTT-TTT-ATT-

TTA-G-3’ to amplify the 3’UTR region. A PCR product coding for the *unc-119(+)* gene was used as a co-injection marker. The *unc-119* gene, including a 2.189 kb upstream region and a 1.228 kb downstream region of the *unc-119a* isoform, was amplified with the forward primer 5′–TCAGTAAAAGAAGTAGAAT–3′ and reverse primer 5′–GAATTTTAACAATACTTC–3′. Final PCR products were injected into the strain EG6699, at a concentration of 50 ng/µL for the reporter and 20 ng/µL for the *unc-119* gene. Microinjection was carried out by injecting DNA into the gonads of young adult hermaphrodites using an Axio-Vert 135 (Zeiss) microscope and FemtoJet microinjection system (Eppendorf). GFP expression was visualized using a Nikon TiE-C2 confocal microscope with epifluorescence (excitation 488 nm, emission 510 nm) and NIS Elements imaging software.

2.3. Fecundity assay

Twenty synchronized L4 worms per condition were transferred to individual NGM plates containing a 15-µL spot of *E. coli* OP50 and kept at 20 °C. Worms were transferred to fresh plates every day until they stopped laying eggs and the eggs were allowed to hatch for one day. One day after the adult was transferred, juveniles and unhatched eggs were counted. The total brood size per condition was calculated as the sum of unhatched eggs and larvae. Fecundity percentages are comparisons of brood size of the mutant to that of WT. Fecundity assays were repeated independently over three biological replicates. Statistical analysis was performed using a Kruskal-Wallis rank sum test.

2.4. Swim Assay

Fifteen synchronized worms (second day of adulthood) per condition were picked into a 20-µL drop of S buffer on a glass slide. Worms were allowed to recover from the transfer for 30 seconds. Subsequently, swimming behavior was recorded for one minute (using a Nikon SMZ745T G-AL

stereo microscope with Nikon digital video camera) and individual body bends (*i.e.* changes in curvature direction of the mid-body) were counted. The swimming assay was repeated independently over three biological replicates. Statistical analysis was performed using a One-way Anova and Tukey *post-hoc* test after sqrt-transformation.

2.5. Pharyngeal pumping rate assay

The pharyngeal pumping rate protocol was based on Raizen *et al.* [28]. At least 10 synchronized worms (second day of adulthood) per condition were transferred to small NGM plates containing a 15-µL drop of fresh *E. coli* OP50. Nematodes were allowed to recover for at least two hours. Grinder pumps in the terminal bulb were counted for 20 seconds every minute for five minutes after which the mean was used to calculate grinder pumps per minute. Pumping rate of worms that were not in the bacterial spot was not counted. An Olympus SZX12 stereo microscope was used to perform the experiment. The pumping rate assay was repeated independently over three biological replicates. Statistical analysis was performed using a Kruskal-Wallis rank sum test.

2.6. Construction of expression plasmids

For the expression of GLB-3a and GLB-3b, complementary DNA (cDNA) of the *glb-3a* and *glb-3b* genes from *C. elegans* strain was used. The *C. elegans* worms were grown as formerly described [8]. After collecting young adult worms, total RNA was produced applying the TriZol method (Invitrogen) followed by LiCl precipitation (Ambion). The OneStep RT-PCR kit (Qiagen) was used for the preparation of the cDNA of the *C. elegans* globins. Cycling conditions were as follows: 30 minutes at 50 °C for the RT reaction, followed by 15 minutes at 95 °C for the activation of the HotStar Taq DNA polymerase, followed by 35 cycles of 60 seconds at 94 °C, 60 seconds at 54 °C and 90 seconds at 72 °C. Afterwards, the cDNA was cloned into the pET23a vector

(Stratagene) using *NdeI* and *XhoI* restriction enzymes (Biolabs, Westburg) and T4 Ligase (Novagen).

2.7. Mutagenesis of recombinant GLB-3

Mutations were introduced by using the Quick-change^{TM} site-directed mutagenesis kit (Stratagene). The truncated GLB-3 has the first 31 amino-terminal residues and the last 13 carboxyl-terminal residues of GLB-3a removed, leaving 3 amino-acid residues before and after the globin domain (GD). This truncated form, hereafter called GLB-3 GD, lacks the N- and C-terminal extensions and is therefore the same for both isoforms. The mutation primers 5'-GGA-ATT-CCA-TAT-GAT-TCA-TTT-ATC-TCC-3' and 5'-GGA-GAT-AAA-TGA-ATC-ATA-TGG-AAT-TCC-3' for the N-terminal extension (including the *NdeI* site) and primers 5'-G-TGG-GCA-AAA-CTC-GAG-CGG-3' and 5'-CCG-CTC-GAG-TTT-TGC-CCA-C-3' for the C-terminal extension (including the *XhoI* site) were used. To confirm the formation of intramolecular disulphide bonding, the cysteine residue on position 70 in GLB-3a was mutated to serine, hereafter called the C70S mutant, using mutation primers 5'-CGT-TCC-CCA-GTT-TCT-CGA-GAA-ATG-TTC-C-3' and 5'-GGA-ACA-TTT-CTC-GAG-AAA-CTG-GGG-AAC-G-3'. In addition, to study the kinetic properties of GLB-3, the histidine residue on position 7 of the E helix (position 94 and 165 in the protein sequences of GLB-3a and GLB-3b, respectively) was mutated to alanine, hereafter called the HE7A mutant, using mutation primers 5'-TGT-GAT-CTC-AAT-TCG-GCT-ACG-AAA-TTG-CTC-TGC-3' and 5'-GCA-GAG-CAA-TTT-CGT-AGC-CGA-ATT-GAG-ATC-ACA-3'. The cDNAs were subsequently cloned, expressed and purified as described above and further.

2.8. Over-expression, purification and sequence analysis

All details for overexpression and purification of the GLB-3a and GLB-3b isoforms, as well as the GLB-3 HE7A, GLB-3 C70S and truncated GLB-3 GD variants are given in the supplementary material (section S1.1). Details on buffer compositions are given in Table S1. Section S1.2 (supplementary material) details the sequence analysis of both isoforms.

2.9. Gel-filtration analysis

Gel-filtration experiments were performed on a Superdex 75 10/300 (GE Healthcare). Both GLB-3 isoforms (~100 μM) and GLB-3 GD (~30 μM) were eluted in buffer C with or without the presence of DTT in the protein solution (see buffer description, Table S1). Due to technical limitations of the detector, absorbance at 370 nm instead of 412 nm was used for the detection of heme proteins.

2.10. UV-Vis absorption and ECD spectroscopy

UV-Vis absorption spectra were taken from the ferric (as-purified) and ferrous (deoxy) form of the GLB-3 isoforms and the different variants in the absence and presence of different potential ligands and redox partners. A detailed description of the experiments is given in the supplementary material, section S1.3.

The electronic CD spectra in combination with UV-Vis absorption spectra of ferric GLB-3 in the presence or absence of DTT were recorded on a Chirascan^{TM}-Plus spectrometer equipped with LAAPD solid-state detector (Applied Photophysics). The instrument was continuously flushed with nitrogen (4 L min^{-1} flow rate), and the measurements were carried out at 20 ºC. For all the recorded spectra, 0.2 cm path length SUPRASIL® quartz sample cells (Hellma BeNeLux) were used. The GLB-3 samples were measured in buffer C in the presence or absence of DTT, in the

spectral ranges 260 – 700 nm and 195 – 260 nm (1 nm bandwidth, 3 seconds nm^{-1}, respectively). The spectra were subtracted by the corresponding buffer.

2.11. Resonance Raman spectroscopy

Resonance Raman (RR) measurements were acquired at room temperature via backscattering using a Dilor XY-800 spectrometer (DILOR) in low-dispersion mode with a liquid nitrogen-cooled CCD detector. A single-frequency Ti:sapphire laser (SolsTis from M-Squared), which is pumped by an 18 W Sprout-G diode-pumped solid-state laser (532 nm) from Lighthouse Photonics, was operated at 830 nm, and subsequently frequency-doubled with an external cavity frequency doubler (ECD-X from M-squared) to obtain 415 nm laser excitation. The spectra were recorded via backscattering with a slit width of 200 μm. Samples were constantly stirred at 500 rpm to avoid local heating and photochemical decomposition. Prior to the measurements, the samples were centrifuged at 10000 rpm for 10 minutes and then loaded into quartz cuvettes with a path length of 1 cm. The power of the laser was set on 12 mW for the as-purified ferric proteins and 1 – 50 mW for the measurements on the CO-bound ferrous proteins. Per protein, 10 spectra were recorded with an integration time of 180 – 240 seconds each to allow removal of the cosmic spikes. This was achieved by removing the highest and lowest data points for each frequency value and averaging the remaining values. The ferrous deoxy and CO-bound ferrous form were prepared as described for the optical absorption spectroscopy measurements. CO-ligated ferrous globins were prepared in parallel with ^{12}CO and ^{13}CO (Cortecnet 99 % ^{13}CO) to assure the same overall conditions. All protein samples had a final protein concentration of ~50 μM in buffer C. The as-purified (ferric) and deoxy (ferrous) form of GLB-3a and GLB-3b were measured in the presence and absence of DTT.

2.12. Electron paramagnetic resonance

X-band continuous-wave EPR measurements were conducted on a Bruker ESP300E spectrometer with a microwave frequency of ~9.44 GHz. The spectrometer is equipped with a liquid helium cryostat (Oxford Inc.), allowing operation from room temperature down to 2.5 K. All EPR spectra were recorded at 10 K with a modulation amplitude of 0.5 mT, modulation frequency of 100 kHz and microwave power of 3 mW. Furthermore, all samples were deoxygenated via a sequential freeze-pump-thaw cycle prior to the EPR measurements and were continuously pumped during the experiment to avoid a background signal of paramagnetic dioxygen ($^3O_2$). Both GLB-3 isoforms were measured in buffer C (Table S1) with or without DTT. All EPR spectra are simulated using EasySpin version 5.2.28, a MATLAB (MathWorks)-based simulation toolbox [29].

2.13. Native mass spectrometry

Both GLB-3a and GLB-3b were buffer-exchanged to an aqueous, volatile ammonium acetate (100 mM NH_4OAc, pH 6.8) solution using P-6 micro Bio-Spin columns (Bio-Rad). Protein concentrations were adjusted to 5-10 µM. The samples were infused via in-house produced gold-coated borosilicate glass capillaries using nano-electrospray ionization (nanoESI) into a Synapt G2 HDMS (Waters, Wilmslow, UK) mass spectrometer where native ion mobility-mass spectrometry (IM-MS) experiments were performed. The instrument was operated in mobility mode and the following crucial parameter settings were applied to retain the native, solution-phase structure of the protein: 1.2 kV capillary voltage, 15 V sampling cone, 1 V extractor cone, 10 V and 2 V collision energy in the trap and transfer collision cell respectively, and 45 V trap DC bias. Pressures throughout the instrument were maintained at 5.0 mbar (backing) and 0.03 mbar (Ar) in

the trap and transfer collision cell. Deconvolution of all spectra was performed manually using MassLynx software (Waters, Wilmslow, UK).

2.14. Flash photolysis and stopped-flow experiments

Attempts were undertaken to measure the CO-binding kinetics of ferrous GLB-3 and GLB-3 HE7A. Full experimental details are given in the supplementary material (section S1.4).

2.15. Redox potentiometry

Redox titrations were performed inside a glovebox which was deoxygenated with N_2. GLB-3a samples were added to a mediator mix solution in a 2.5 mL polystyrene macrocuvette (BRAND) to achieve a final ~10 μM protein concentration. The following redox mediators were used: phenazine methyl sulfate (E_m = 80 mV), 2-methyl-1,4-naphthoquinone (E_m = 10 mV), potassium indigotetrasulfonate (E_m = −46 mV), 2-hydroxy-1,4-naphthoquinone (E_m = −137 mV), and disodium anthraquinone 2,6-disulfonate (E_m = −184 mV) at concentrations between 1 and 5 μM following the procedure in [30]. The mediators act as a redox buffer and equilibrate the potential between the protein and the electrodes. Stock solutions of the mediators were prepared in 100 mM sodium phosphate buffer pH 7. Titrations were conducted at room temperature by stepwise addition of a 0.1 M sodium dithionite solution *via* a 1 mm I.D. Teflon tube (Bola) using a NE-1000 Programmable Single Syringe Pump (KF Technology). The sample was stirred continuously using a magnetic stirrer built into the cuvette holder. After each injection the system was allowed to equilibrate for several minutes, and a UV-Vis absorption spectrum was taken using a Spectronic Genesys 6 UV-vis spectrophotometer (Thermo Fisher Scientific). Simultaneously, the open circuit potential between a Leak-Free Ag/AgCl 3M Reference Electrode (Innovative Instruments, Inc) and a 4×25 mm Pt plate (Goodfellow, 99.95 % pure and 1 mm thick) submerged in the solution was monitored using a VersaSTAT 3 potentiostat (Princeton Applied Research). The potentials

were converted to a value versus standard hydrogen electrode (SHE) by a correction factor of +210 mV. The change in the heme oxidation state was monitored by the change in the Q bands at 530 and 560 nm. The total absorbance at each wavelength is given by the sum of the fraction oxidized (Fe^{3+}) and the fraction reduced (Fe^{2+}). Both fractions were determined by calculating their molar extinction coefficients at 530 and 560 nm according to Lambert–Beer's law. The titration curves were fit to the Nernst equation: $E = E_{\mathrm{m}} + 2.303\ \frac{RT}{nF}\ \log\frac{[\text{oxidized}]}{[\text{reduced}]}$, where E is the measured equilibrium potential at each titration point, E_{m} is the redox potential of the Fe^{3+}/Fe^{2+} couple, R is the gas constant (8.314 J mol^{-1} K^{-1}), T is the experimental temperature in Kelvin, n is the number of electrons in the half-reaction, F is the Faraday constant (96485 C mol^{-1}), and [oxidized]/[reduced] is the ratio of oxidized to reduced species. MATLAB (MathWorks) was used to analyze the data and the E_{m} value is expressed as the mean ± the standard deviation of the mean.

3. RESULTS

3.1. Sequence analysis

Figure 1 shows a comparison between the protein sequence of the globin domain (GD) of GLB-3 and those of the previously characterized *C. elegans* globins GLB-1, 5, 6, 12, 13, 26 and 33 [11,16-23]. Full-length GLB-3b consists of 282 amino-acid residues whereas GLB-3a is the shorter isoform and contains 210 amino-acid residues (Figure S1). GLB-3 features all characteristics of a standard globin since all globin-typical amino-acid residues for genuine globins are conserved. Both GLB-3 isoforms are found to possess a single GD and exhibit the canonical 3/3 α-helical Hb fold formed by the A-G-H and B-E-F helices, including a new member to the M family [1,2]. Intriguingly, GLB-3b and GLB-3a possess 12 and 9 cysteine residues, respectively, of which 8 are localized in the GD (Figure 1 and S1). A search in the globin database resulted in the discovery

that ~52 %, ~53 % and ~55 % of the globins in the M, S and T family, respectively, are found to have at least one cysteine residue in their GD. Only ~0.04 % globins with at least 8 cysteine residues in the GD are found in the M family, in contrast to the S and T family where no such globins were found. More specifically, these particular globins in the M family are predominantly found in the Wormbase nematode database [31]. ~97 % of the globins found in the Wormbase contain at least one cysteine residue in the GD, with ~3 % possessing at least 8 cysteine residues in their GD, including GLB-3 (Figure S2).

Furthermore, GLB-3b is predicted to be both myristoylated and palmitoylated (Figure S1B). Both post-translational modifications promote stable membrane anchoring and are also found in other *C. elegans* globins (Table 1). The N-terminal myristoylation site in GLB-3b is predicted with very high confidence (96 %), found at the second Gly residue. Palmitoylation was found for GLB-3b at the cysteine residues on positions 206 or 207 (denoted as Cys206 and Cys207) (Figure S1). GLB-3a, on the other hand, is predicted to be non-myristoylated due to the absence of the first two N-terminal exons and partly the third exon. However, like GLB-3b, GLB-3a is also predicted to have a palmitoylation site (Cys134 or Cys135) and interestingly, GLB-3a reveals an additional N-terminal mitochondrial targeting site (MTS) with a probability of 80 %.

Figure 1. Protein alignment of *C. elegans* globins. GLB-3 (accession number CAR81336) is aligned with the *C. elegans* globins that are previously characterized: GLB-1 (accession number CAA77458), GLB-5 (A3RMS5), GLB-6 (CCD65109), GLB-12 (CAA86764), GLB-13 (CAA92164), GLB-26 (CAA99921) and GLB-33 GD (CTQ86984). The amino-acid residues preceding and following the protein sequence are shown as numbers in brackets. The globin domain of GLB-3a is shown, which is identical for GLB-3b (103 preceding and 15 amino-acid residues following). Sperm whale myoglobin (swMb with accession number BAF03579) with the corresponding helices and topological positions are shown above the protein sequences. Conserved residues at buried sites in the helices are indicated with a capital letter according to [32]. The cysteine residues in the globin domain of GLB-3 are shown in red. The key residues at position CD1 and F8 are highlighted in blue and green respectively and the E7 position is marked in purple.

3.2. *In-vivo* localization of GLB-3 and functional implications

By using a GLB-3 translational reporter strain we revealed that GLB-3 is expressed in the reproductive and the nervous system. Within the reproductive system, GLB-3 could be localized in vulval muscle cells (Figure 2c) and the proximal part of the gonadal sheet (Figure 2d). This expression pattern links well to the observation that mutation of *glb-3* leads to a 99 % reduction in fertility which points at a crucial role for GLB-3 in wild-type (WT) reproduction (Figure 2e). Heterozygotes also show a decreased brood size compared to WT, but the large number of

unhatched eggs is at least partially caused by the non-viability of the homozygous nT1 balancer [33]. In the nervous system, GLB-3 is expressed in a selection of head and tail neurons and the nerve cords along the body (Figure 2a and 2b). Our observations with the GLB-3::GFP translational reporter agree with expression data available from RNA-seq based single-cell expression analysis (CeNGEN project) [34]. Based on the neuronal expression pattern and the previously described roles of these neurons, we screened for two behavioral phenotypes: motility – quantified as body bend rate during swimming – and pharyngeal pumping rate. The absence of a functioning *glb-3* gene causes a strong reduction of the rates of both behaviors. *glb-3* mutants show a 52 % reduction in swimming rate compared to the WT (Figure 2f), while pharyngeal pumping rate is decreased by 49 % (Figure 2g). Heterozygous *glb-3* mutants show no significant decrease in pumping rate or body bends compared to the WT, suggesting that one functional copy of *glb-3* is sufficient for normal neuronal functioning.

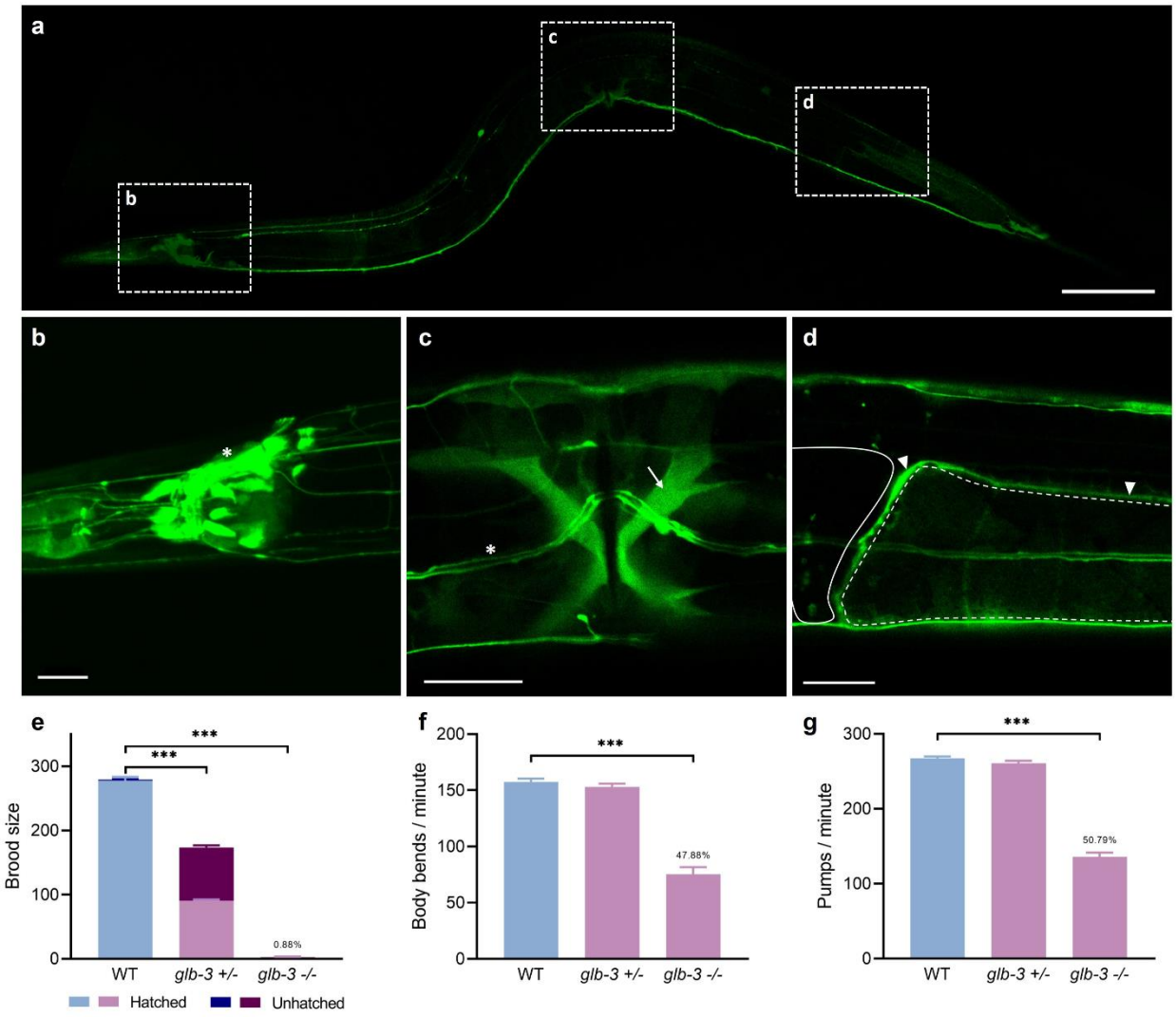

Figure 2. GLB-3 expression pattern and mutant phenotypes. a) Whole worm overview (scale bar = 100 µm). GLB-3 is expressed in neurons, the vulva and the gonadal sheath. Enlargements in (b-d). b) GLB-3 expression in head neurons (asterisk) (scale bar = 20 µm). c) GLB-3 expression in vulval muscles (arrow) and ventral cord neurons (asterisk) (scale bar = 20 µm). d) GLB-3 expression in the proximal part of the gonadal sheet (arrowhead). Oviduct (dashed line) and spermatheca (full line) are also indicated (scale bar = 20 µm). e-g) *glb-3* knockout leads to a severely reduced fecundity (e), swimming rate (f) and pharyngeal pumping rate (g). ***P < 0.001. Data are represented as mean ± SEM.

3.3. *In vitro* protein stability and protein folding

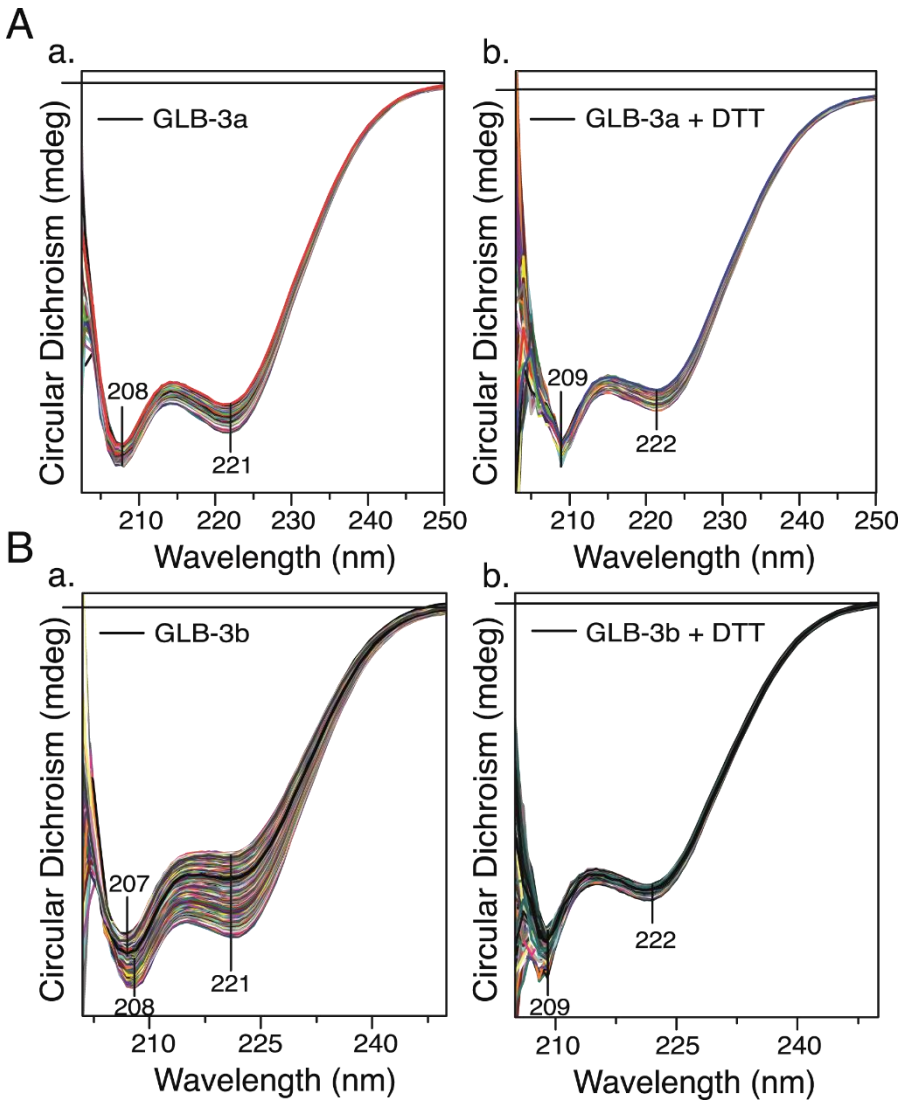

Figure 3. CD spectra of ferric GLB-3a and GLB-3b. A) Far-UV spectra of ferric GLB-3a without (a) and with (b) DTT. The time difference between the first and last spectrum is 8 hours. B) Far-UV spectra of ferric GLB-3b without (a) and with (b) DTT. The time difference between the first and last spectrum is 18 hours. The black trace corresponds to the measurement after 8 hours.

In line with what is expected for globins, the circular dichroism (CD) spectra of both GLB-3 isoforms display double minima around 208 and 222 nm, typical for protein structures that are mainly α-helical (Figure 3). Comparison of the far-UV CD spectra of the full-length GLB-3 isoforms with that of the truncated GLB-3 GD variant, indicates the presence of loop regions in

the extensions (Figure S3). While the far-UV CD spectra of GLB-3a change only slightly over the course of 8 hours (Figure 3Aa), a strong time-dependent change is observed for GLB-3b, indicating protein denaturation and aggregation (Figure 3Ba). In both cases, addition of DTT to avoid formation of intermolecular disulphide bridges, leads to increased protein stability (Figure 3A,Bb). Interestingly, the GLB-3b HE7A variant could not be stabilized over longer time with DTT, implying also a role of the E7 ligand in protein stabilization (Figure S4B).

The visible CD region reveals no significant heme loss over time for the two GLB-3 isoforms (Figure S5). Interestingly, GLB-3b and GLB-3a exhibit negative ellipticity in the Soret-Q spectral regions (Figure S5), in contrast to what has been reported for ferric Mb [35]. This reveals an altered interaction of the heme group with its surrounding (see later). This negative ellipticity is also observed in the GLB-3 HE7A and GLB-3 GD variants (Figure S3, S4).

3.4 Protein multimerization

Both GLB-3a and GLB-3b were subjected to native mass spectrometry (MS) analysis in order to determine the oligomerization state with and without DTT. No differences are observed between the MS spectra with and without DTT for GLB-3a (Figure 4A). As clearly visible, both spectra display the same charge state distribution that represents monomeric GLB-3a in both folded (low charge states; high m/z) and partially unfolded state (high charge states; low m/z). Additional to these monomers, GLB-3a shows the presence of a very minor fraction of dimers (~3400 m/z), with a slightly higher contribution of dimers in the absence of DTT. This indicates that the dimerization is stabilized by disulphide bonds, which also follows from the gel-filtration experiment (Figure 5). We must mention that during centrifugation, in the absence of DTT, we observed pellet formation due to protein aggregation. Thus, it is conceivable that the disulphide bonded dimer aggregates and is removed prior to the experiment, explaining its negligible

fraction in the mass spectrum. The obtained experimental molecular weight (MW) of the monomer GLB-3a (25047.05 ± 0.67 Da) is in good agreement with the theoretical MW (25003 Da).

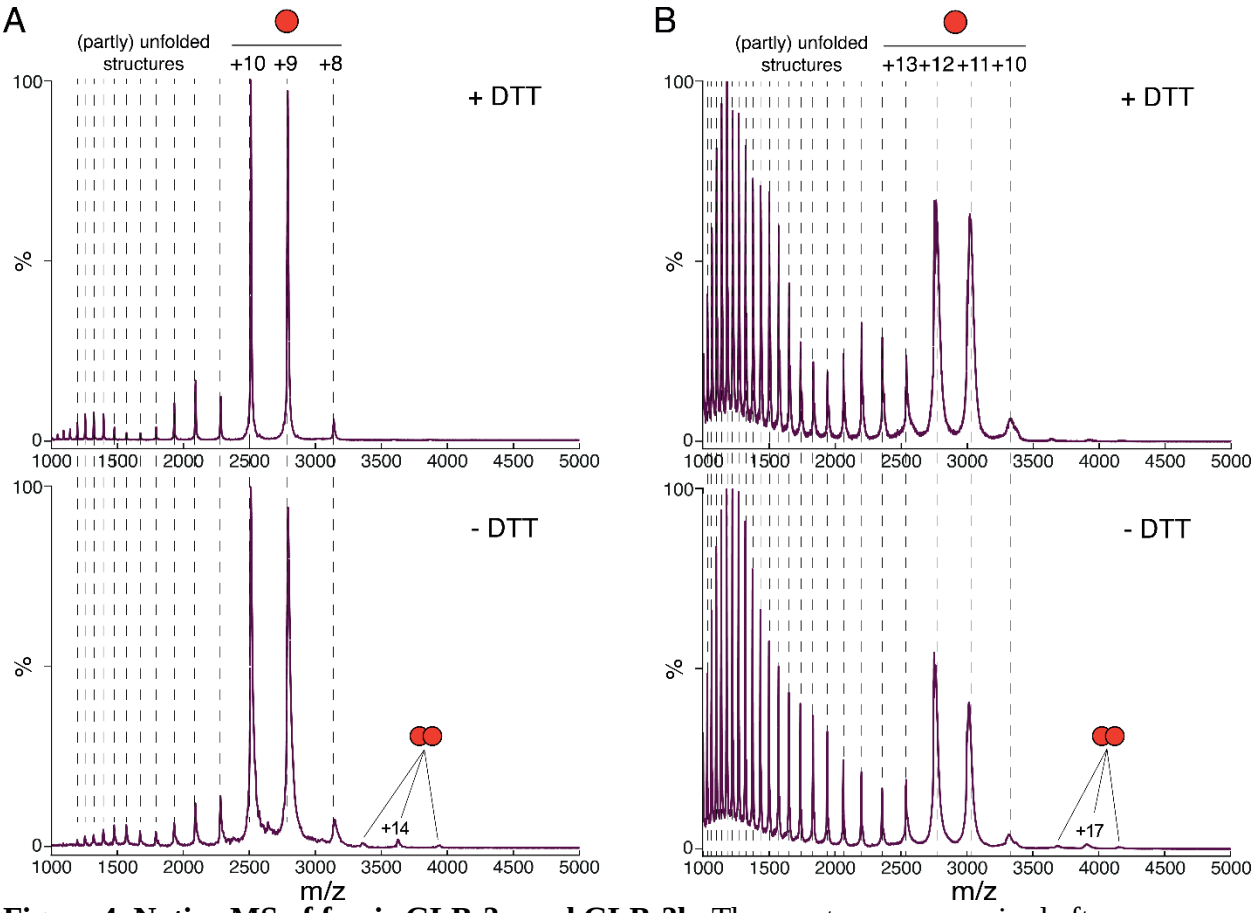

Figure 4. Native MS of ferric GLB-3a and GLB-3b. The spectra were acquired after purification of A) GLB-3a and B) GLB-3b with (top) and without (bottom) the addition of DTT. A) Both spectra of GLB-3a are similar and display a multimodal charge state distribution whereby the native monomers (+10, +9, +8) and the (partly) unfolded structures are indicated. Additional to the monomeric species, the spectra also show minor peaks (> 3500 m/z; 1-2 % intensity) of dimers. B) The spectrum of GLB-3b at the top (+DTT) shows a monomeric peak series (+13, +12, +11, +10) and a reasonable fraction of the protein (partially) unfolded. Without the addition of DTT (bottom), the spectrum again displays monomers and a high fraction of (partially) unfolded protein. The dimer fraction (> 3500 m/z) compared to the native monomer fraction is ~1-2 % in intensity in absence of DTT, whereas the addition of DTT reduces the intensity to less than 1 % (see peaks marked with double circles).

The MS spectra acquired for GLB-3b with and without DTT also show mostly monomers (Figure 4B), with a very small contribution of dimers. The latter fraction is again underestimated

due to the prior centrifugation step. However, in contrast to GLB-3a, a reasonable fraction of (partially) unfolded species is observed for GLB-3b below m/z 2500, and in particular below m/z 1700, indicating the presence of a disordered region, likely the flexible N-terminal extension. These unfolded species were still observed when other types of buffer (with different detergents and varying NaCl concentrations) were used (data not shown). The addition of DTT results in a slightly higher intensity of the native monomer peaks. The experimental MW of the monomer GLB-3b is found to be 32949.93 ± 0.25 Da, which is in agreement with the theoretical MW (32902 Da).

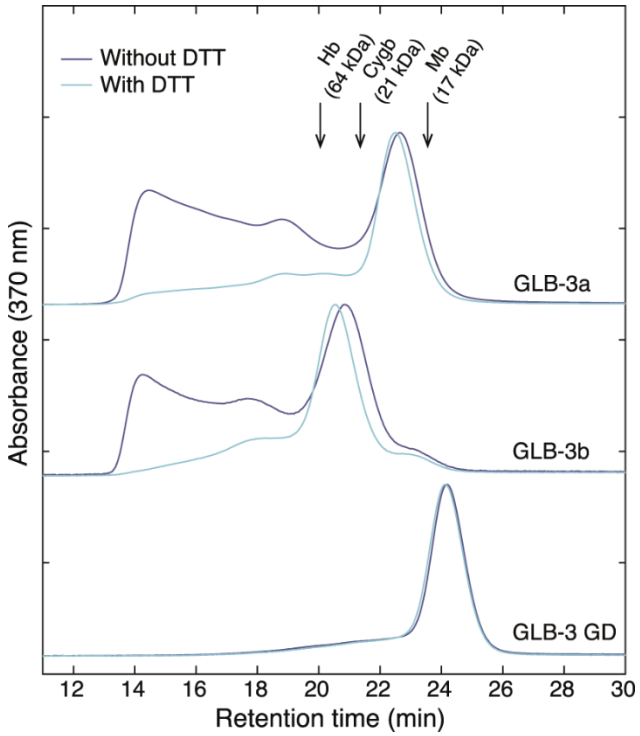

Figure 5. Gel-filtration chromatography of ferric GLB-3a, GLB-3b and GLB-3 GD. Normalized elution profile from gel-filtration of ferric GLB-3a, GLB-3b and GLB-3 GD with (light blue) and without (dark blue) DTT. Absorbances were measured at 370 nm (heme) and 280 nm (aromatic amino-acids, not shown). As standards, myoglobin (monomer), cytoglobin (dimer) and hemoglobin (tetramer) are also loaded into the column and the positions of the elution peaks are indicated by the arrows. DTT clearly decreases the presence of formed aggregates in the GLB-3a and GLB-3b protein batch, resulting in a more (visually) stable protein solution.

The reduction of protein aggregation after the addition of DTT is confirmed via gel-filtration (Figure 5). GLB-3a (25 kDa) has a retention time consistent with a monomer confirming the MS data. Surprisingly, GLB-3b (33 kDa) shows a much earlier retention time (close to Hb), while native mass spectrometry shows it to be a monomer in solution. A similar effect has been observed for human cytoglobin, where the flexible N- and C-terminal extensions of the monomeric protein are responsible for a large increase in hydrodynamic volume relative to a globular protein, resulting in the apparent elution as a dimeric globin [36]. This suggests that GLB-3b is not a globular protein with the flexible long N-terminal extension tightly packed to the globin core. The gel-filtration experiment of the truncated GLB-3 GD variant (19 kDa), lacking the extensions, reveals indeed a hydrodynamic diameter similar to a classical monomer. Note that the absence of significant amounts of oligomers in the elution profile of the GLB-3 GD batch is likely caused by the timing of the experiment, *i.e.* immediate gel-filtration after protein purification leaving not enough time for protein aggregation.

3.5 Spectroscopic analysis of the heme pocket of ferric and ferrous GLB-3

In order to evaluate the heme pocket in both ferrous and ferric form of the GLB-3 isoforms, different spectroscopic analyses were performed. The UV-Vis absorption spectra of ferric (as-purified) and ferrous (deoxy) GLB-3a are shown in Figure 6A. For the ferric form, direct comparisons with the CD spectra are given in Figure S5. The UV-Vis absorption spectra are similar for GLB-3b with or without DTT (Figure S5 for ferric form). Both ferric and ferrous deoxy form exhibit an optical absorption spectrum typical of low-spin (LS) heme iron that is hexacoordinated (6c/LS), with the Soret and the Q_α and Q_β bands, respectively, at 413 nm, 567 nm and 533 nm for the ferric form, and at 426 nm, 560 nm and 530 nm for the ferrous deoxy form. Based on the sequence alignment the distal ligand is most likely the endogenous E7His (Figure 1, Figure 8B for

structure visualization). A similar conclusion is drawn from the high-frequency region of the resonance Raman (RR) spectra (Figure 6C), in which marker bands are observed at ν_4 = 1376 cm^{-1}, ν_3 = 1505 cm^{-1}, ν_2 = 1580 cm^{-1} and ν_{10} = 1635 cm^{-1} for the ferric form, typical of a 6c/LS ferric form, and at ν_4 = 1362 cm^{-1}, ν_3 = 1494 cm^{-1}, ν_2 = 1584 cm^{-1} and ν_{10} = 1621 cm^{-1}, typical of a 6c/LS ferrous form.

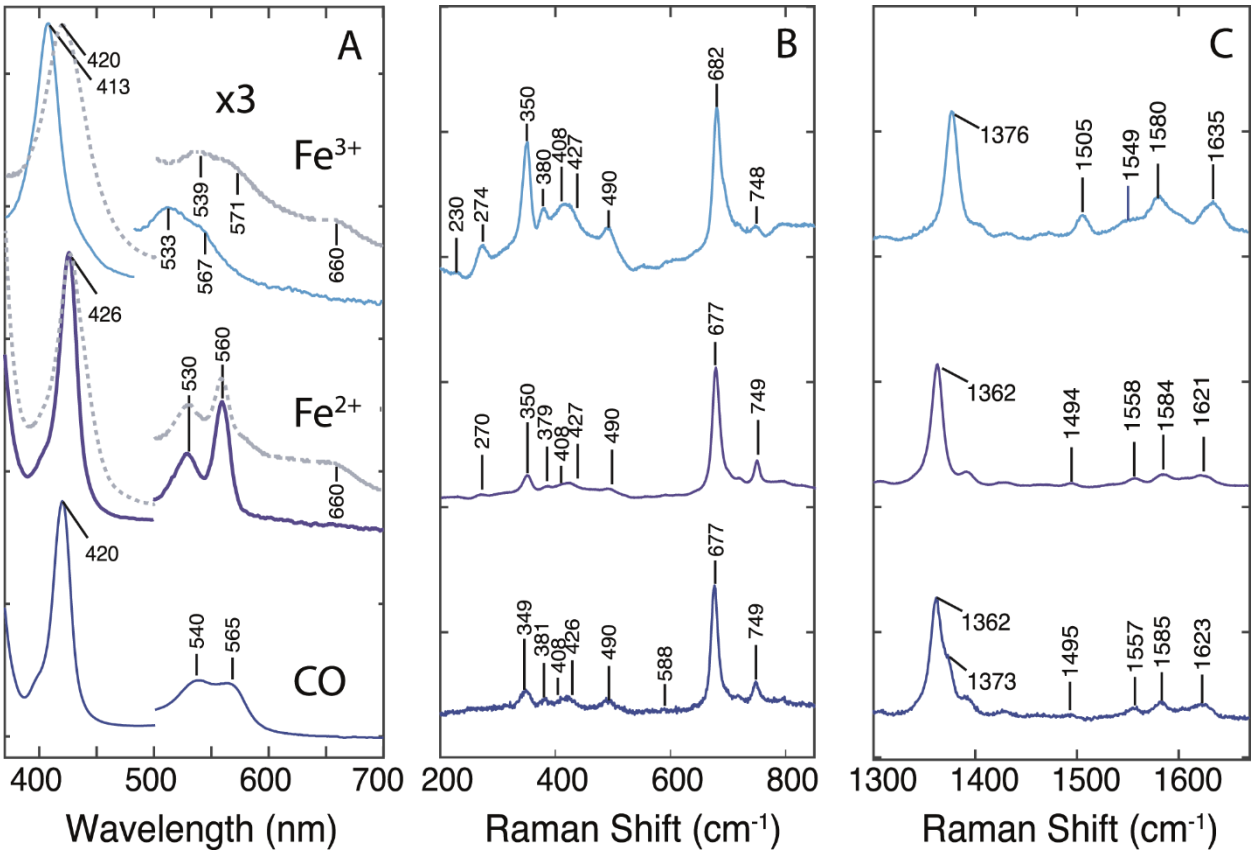

Figure 6. UV-Vis absorption and RR spectra of GLB-3a. A) Normalized UV-Vis absorption spectra of GLB-3a (full lines) and GLB-3a HEA7 (dotted lines) in the as-purified ferric form, the ferrous deoxy form and the ferrous CO-ligated form at pH 7.5 with DTT (similar spectra without DTT and for GLB-3b). The Q bands are magnified by a factor of 3. B) Low-frequency region and C) high-frequency region of the RR spectra of GLB-3a in the as-purified ferric form recorded at 12 mW laser power, the ferrous deoxy form recorded at 12 mW laser power and the ferrous CO-ligated recorded at 1 mW laser power. The protein solution is measured in 50 mM Tris-HCl pH 7.5, 500 mM NaCl and DTT. The results are similar without the addition of DTT, and for GLB-3b. The CO measurements are only performed with DTT.

The low-frequency region (Figure 6B) of the RR spectra displays several bending modes from the vinyl $\delta(C_\beta C_a C_b)$ and propionate $\delta(C_\beta C_c C_d)$ substituents of the heme [37]. The frequency of these modes is related to the strength of the hydrogen bonds between the propionate and vinyl groups with nearby amino-acid residues in the heme pocket. The propionate bending mode is situated around 379 – 381 cm^{-1} in the ferric and ferrous deoxy form, indicating a strong hydrogen bond interaction between the propionate side chains and nearby amino-acids [37]. The broad band around 416 cm^{-1} consists of signals around 409 cm^{-1} and 427 cm^{-1} (Figure S6), which are assigned to the vinyl bending modes. The deoxy form display a slightly higher propionate bending mode at 383 cm^{-1}, pointing to a higher stabilization in the heme compared with the ferric form. Note that there is no detectable out-of-plane-mode γ_7 observed (288 – 312 cm^{-1}), indicating a lack of out-of-plane distortions of the heme [37]. This is characteristic for LS complexes, where the iron is in the heme plane due to the axial ligation to two ligands. Moreover, because of the hexacoordination no ν_{Fe-His} mode is observed (200 – 250 cm^{-1}) in the ferric and deoxy form [38].

Figure 7a-d displays the continuous-wave electron paramagnetic resonance (CW EPR) spectra of ferric GLB-3a with and without DTT and GLB-3b with DTT. Due to protein instability, GLB-3b was not measured without DTT. DTT is added in two ways to GLB-3a: no DTT is added right after the purification process but added ~1 hour prior to the EPR measurements and the sample is then stored at 4 °C (Figure 7b), or DTT is added immediately after purification and thus the sample is stored for a longer time in a reducing environment (Figure 7c). The EPR spectra show the expected feature of a 6c/LS (S = ½) ferric heme with the principal g-values determined by spectral simulations shown in Table 2. The high-field feature g_x (g_{min}) is not observable because of large g-strain effects and therefore estimated using the assumption that $g_z^2 + g_y^2 + g_x^2 \approx 16$ [39]. Intriguingly, three 6c/LS forms are detected, denoted as LS1, LS2 and LS3. These three forms can

be ascribed to the F8His – Fe^{3+} – E7His conformation with a different relative arrangement of the imidazole planes of the axial histidine ligands [40,41].

The LS3 form shifts (to LS3') and diminishes immediately after addition of DTT (Figure 7b) and almost disappears after long storage in DTT (Figure 7c), suggesting that the three observed LS complexes correspond to forms without (LS1 and LS2) and with (LS3) disulphide bridges. Since EPR experiments of heme proteins demand a high concentration (~1 mM) in which the surface cysteine residues may come close to each other, intermolecular disulphide bonds are likely to be formed. This is confirmed by MS (Figure S11). Because the monomers are more closely packed, the heme pocket (and thus its EPR parameters) can be affected by such intermolecular bridges. Intramolecular disulphide bridges may also play a role, since at lower GLB-3a concentration (~450 µM) LS3 is still present in the absence of DTT (Figure S9a and b).

The principal *g*-values of the LS ferric heme centres found for GLB-3 are typical for $(d_{xy})^2(d_{xz},d_{yz})^3$ configurations. The LS1 and LS2 complexes of GLB-3 are referred to as normal rhombic or type-II EPR signals [39]. In contrast, the LS3 (and LS3') complex of GLB-3 shows a very high g_{max} > 3.2 value, resulting in a large *g*-anisotropy, making it difficult to observe g_x (g_{min}). This complex is referred to as type-I EPR signals [39]. In line with the UV-Vis data (Figure 6A), no signal due to a HS ferric heme center is observed in the EPR spectra of the GLB-3 protein samples (Figure S9).

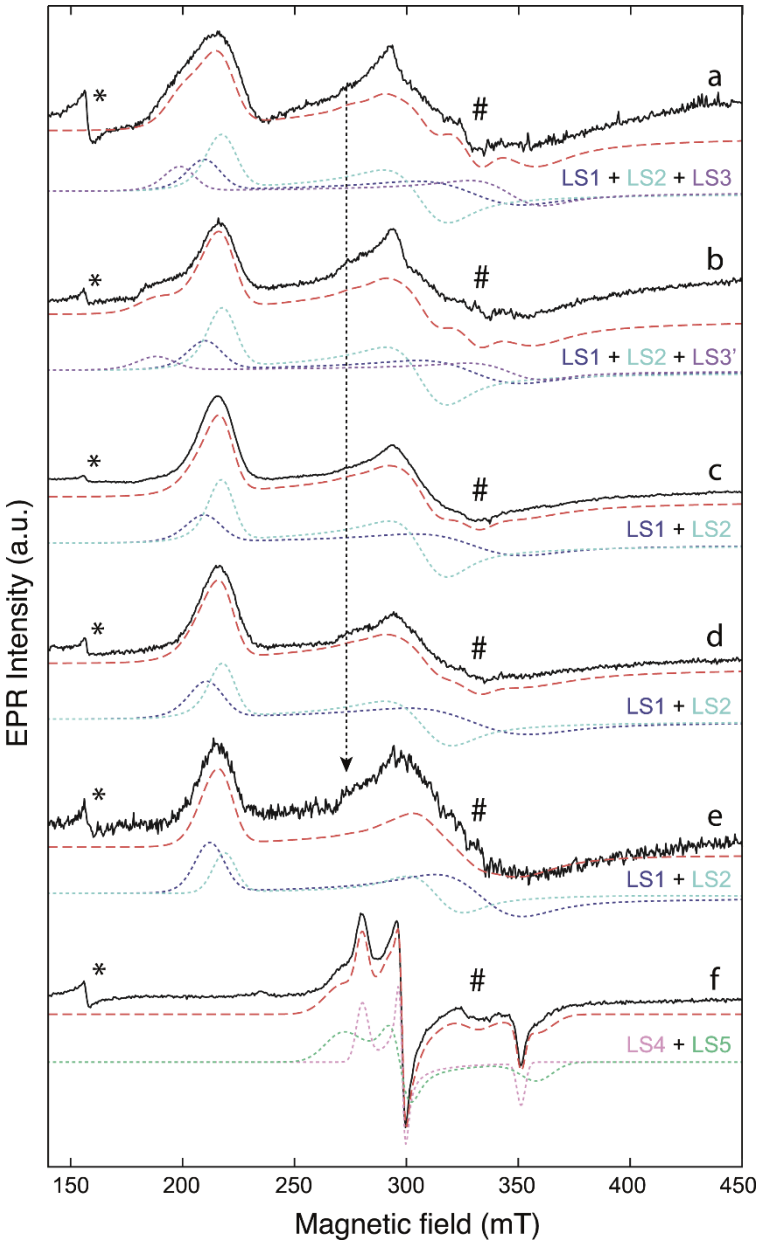

Figure 7. **X-band EPR spectra of ferric GLB-3a and GLB-3b.** Normalized X-band CW-EPR spectra of a frozen solution at pH 7.5 of a) ferric GLB-3a without DTT, b) ferric GLB-3a with DTT added ~1 hour prior to the EPR measurement, c) ferric GLB-3a with DTT added immediately after the purification process, d) ferric GLB-3b with DTT, e) ferric GLB-3a C70S without DTT and f) ferric GLB-3a HE7A without DTT measured at 10 K. The corresponding simulations are shown shifted down from the experimental spectra in red dashed lines with the individual LS components shown as dotted lines. An additional signal, indicated by the arrow, is observed at g = 2.46, most probably originating from an exogenous ligand from the buffer solution that has coordinated with the heme cofactor. *indicates the contribution of a non-heme iron Fe^{3+} and # a Cu^{2+} background signal.

Table 2. The principal *g*-values of GLB-3 and other ferric proteins. EPR parameters of GLB-3 with and without DTT compared to heme proteins, with a histidine or thiolate as an axial ligand, reported to participate in redox reactions, more specific electron transfer. The contribution of each simulated LS form is given. n.d. = not determined, *DTT added prior to EPR measurement, **DTT added right after protein purification, #estimated based on $\sum g_i^2 \approx 16$.

Species	g_z ±0.02	g_y ±0.03	g_x ±0.04	Contribution ±3 %	Axial ligands	Ref.
GLB-3a					His/His	
LS1	3.18	2.01	1.37#	30 %		This work
LS2	3.07	2.18	1.36#	40 %		This work
LS3	3.36	1.93	1.01#	30 %		
*GLB-3a + DTT**					His/His	
LS1	3.17	2.01	1.36 #	32 %		This work
LS2	3.07	2.18	1.35#	48 %		This work
LS3'	3.54	1.93	n.d.	20 %		
*GLB-3a + DTT***					His/His	
LS1	3.17	2.01	1.38#	41 %		This work
LS2	3.07	2.17	1.36#	59 %		This work
*GLB-3b + DTT***					His/His	
LS1	3.16	2.01	1.41#	51 %		This work
LS2	3.07	2.17	1.37#	49 %		This work
GLB-3a C70S					His/His	
LS1	3.15	1.99	1.43#	65 %		This work
LS2	3.07	2.14	1.35#	35 %		
*GLB-3a C70S + DTT**					His/His	
LS1	3.14	1.97	1.50#	63 %		This work
LS2	3.07	2.18	1.35#	37 %		
*GLB-3a C70S + DTT***					His/His	
LS1	3.15	1.97	1.48#	59 %		This work
LS2	3.08	2.17	1.32#	41 %		
NGB					His/His	
LS SH	3.10	2.17	1.30			[40,41]
LS S-S	3.26	2.06	1.05			[40,41]
mNGB	3.12	2.15	1.29		His/His	[41]
CYGB	3.20	2.08	1.20		His/His	[41]
GLB-26	3.25	n.d.	n.d.		His/His	[21]
Cytochrome b_5	3.03	2.23	1.43		His/His	[42]
Barley Hb	3.02	2.22	1.48		His/His	[43]
PpcA cytochrome heme I	3.24	1.98	1.22		His/His	[44]
GLB-3a HE7A					Cys^-/His?	
LS4	2.49	2.27	1.88	63 %		This work
LS5	2.41	2.26	1.91	34 %		This work
NGB HE7A + H_2S	2.48	2.29	1.85		H_2S/His	[45]
R. sulfidophilum SoxAX					Cys^-/His	
LS	2.52	2.23	1.84			[46]
LS	2.58	2.30	1.87			[46]
Cyt c M80C	2.56	2.27	1.85		Cys^-/His	[47]

3.6. Evaluating potential intramolecular disulphide-bridge formation

In order to identify candidate Cys residues for intramolecular disulphide-bridge formation, homology modelling of the tertiary structure of the globin domain (GD) of GLB-3 was performed by means of SWISS-MODEL [48-52]. Figure S1C and Figure S12 (supplementary material) indicate the modeled region. Note that the model does not include the N- and C-terminal extensions and hence only a homology model of GLB-3a is presented since GLB-3b is identical in that region. The model is constructed based on the known crystal structure of human neuroglobin (PDB ID: 1OJ6 [53]). Despite that *C. elegans* GLB-6 (PDB ID: 3MVC [19]) gives the highest sequence identity (25.5 %) with GLB-3 according to SWISS-MODEL and other programs like Phyre^2 [54] and ModBase [55], it was not possible to position the heme co-factor correctly in the predicted GLB-3 model based on the GLB-6 template. Therefore, human Ngb is chosen based on the spectroscopic similarities and because the bis-histidyl ligated heme structure of GLB-6 is reported to be closely related to the crystal structure of human Ngb [19]. The QMEAN-Z score, which is an estimation of the degree of nativeness, is -2.55 indicating a good agreement between the model structure and experimental structures of similar size [51]. Verify3D showed that 80.27 % of the amino-acid residues have a score higher than 0.2 [56,57]. ProSa-Web analysis confirms these results through a negative Z-score of -4.34 for the global molecule [58,59]. Further checks about the stereochemical quality are evaluated by Procheck that reveals the Ramachandran plot, showing 99.2 % of all amino-acid side chain angles are in the allowed regions and 0.7 % in disallowed region [60,61]. All these data confirm that this predicted model is reliable.

The homology model is visualized in Figure 8A, showing the characteristic α-helical three-over-three globin fold. The heme iron is ligated by the distal His94(E7) on the E helix and the proximal His127(F8) on the F helix (Figure 8B,C), with the heme being further surrounded by hydrophobic

and aromatic residues (Phe74, Phe139, Phe146, Leu63, Leu97, Leu98, Leu101, Leu142, Met73, Met130, Val123, Val138, Ile177) and a number of polar residues located at a somewhat greater distance (Gln75, Asp90, Asn131, Lys76, Glu132, Lys133, Asn129, Ser93). The homology model provides a better insight into the location of the Cys residues in the globin domain. The surface Cys residues at positions 89, 134, 135, 155, 168 are solvent-exposed. Disulphide-bridge formation with nearby proteins is possible at high protein concentrations since their thiol side chains are directed to the solvent. The buried Cys residues are found at positions 70, 99, 120. Since the N- and C-terminal extensions are not included in the model, Cys207 from GLB-3a and Cys30, Cys62, Cys70 and Cys279 from GLB-3b are not considered in the model.

According to the predicted GD model, the only Cys residues that can possibly form an intramolecular disulphide bond are Cys134 or Cys135, positioned on the solvent-exposed flexible FG loop with Cys70 on the C-helix. This finding remains if several other templates (CYGB, GLB-12 and GLB-6) are used to construct a GLB-3a model (data not shown), meaning that it is not solely an artefact of the NGB template. To accurately predict the secondary structure of the N- and C-terminal extensions, the popular JPred4 protein secondary structure prediction server [62] was used (Figure S13). The N- and C-terminal extensions of both isoforms are predicted as disordered regions with a high confidence level. This is confirmed by the AlphaFold structure prediction [63,64] of the GLB-3a and GLB-3b apoproteins (Figure S14).

In order to check whether Cys70 could be involved in an intramolecular disulphide bridge the GLB-3 C70S variant was constructed, revealing the absence of the LS3 complex in the corresponding EPR spectrum (Figure 7e and S10). The same effect was induced by addition of DTT, and Cys70 is thus confirmed to play a role in the disulphide-bridge formation. The contribution of LS1 dominates the EPR spectrum of the C70S variant of GLB-3a (Table 2).

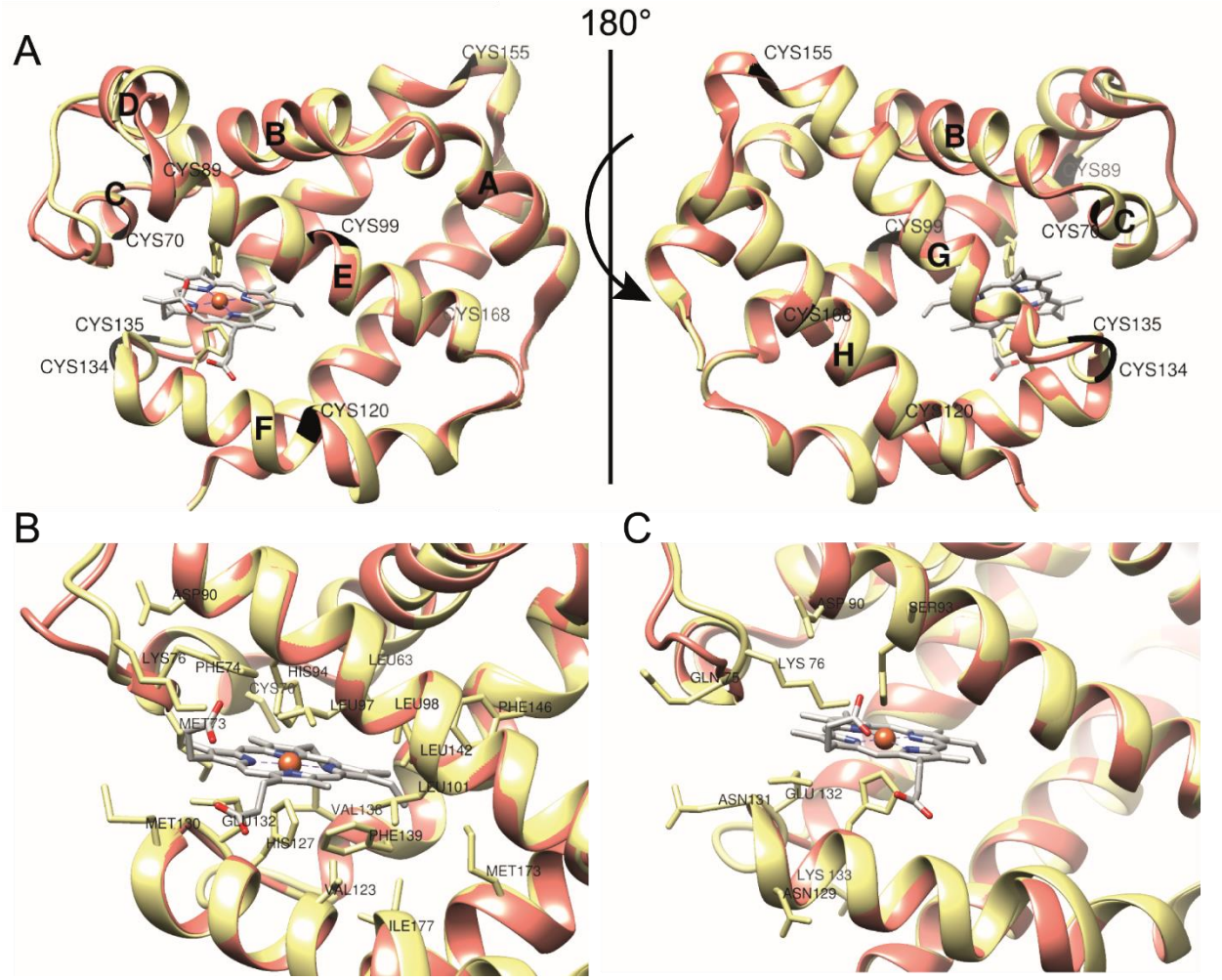

Figure 8. The three-dimensional model of GLB-3a. A) Superimposition of GLB-3a (yellow) and NGB (PDB 1OJ6) (pink) with the heme cofactor. The cysteine residues of GLB-3a are highlighted in black and the helixes are illustrated with the corresponding letter (from A to H). Note that the 1OJ6 NGB crystal structure is the Cys46Gly/Cys55Ser/Cys120Ser mutant and thus is an example of NGB in a very reducing environment. B-C) Zoom-in on the heme pocket. B) Illustrates all amino-acid residues of GLB-3a less than 0.5 nm from the heme and C) reveals the presence of the polar amino-acid residues less than 0.6 nm from the heme (Visualization and analysis using UCSF Chimera [65])

3.7 Exogenous and endogenous distal ligand binding to heme iron

All spectroscopic evidence points to a distal endogenous E7His (His94) ligation to the heme iron in both the ferric and ferrous form (Figure 8B). In order to further explore the effect of the distal ligation, the GLB-3 HE7A mutant was constructed. Since the Ala residue cannot ligate iron, this

point mutation was expected to induce a high-spin (HS) pentacoordinated heme form (5c/HS). Surprisingly, the UV-Vis absorption spectra indicated the observation of a 6c/LS form with the Soret band at 420 nm and the Q_α and Q_β bands at 571 and 539 nm (ferric form), and a Soret band at 426 nm with the Q_α and Q_β bands appearing at 560 and 530 nm (ferrous deoxy form), respectively (Figures S4C, Figure S22C). In all cases, a band is found around 660 nm, potentially being a charge-transfer (CT) band. The absorption spectrum resembles that of the cytochrome c mutant in which the axial heme ligand Met80 is replaced by Cys giving rise to a CT band around 660 nm [66]. The possible distal ligation of a Cys residue is corroborated by the EPR data of ferric GLB-3a HE7A (Figure 7f). The earlier observed contributions of LS1-3 are replaced by two overlapping EPR contributions, LS4 and LS5. A minor feature points out the presence of a small amount of a HS form of the globin (Figure S9). The principal *g*-values of LS4-5 are in fair agreement with the sulfide-treated NGB HE7A mutant and heme proteins with a cysteinate or similar thiolate axial ligand ([45,46], Table 2). This indicates a strong rearrangement of the heme pocket, and this may be linked to the earlier observation that this point mutation considerably decreased the time-dependent protein stability in the presence of DTT for GLB-3b (Figure S4A,B). Since some of the known functions of globins involve the binding of small diatomic ligands, the interaction of ferrous GLB-3 with O_2 and CO was probed. Unfortunately, due to the extremely fast auto-oxidation of GLB-3, the oxy form could not be studied. In contrast, stable CO-ligated complexes could be obtained as confirmed by UV-Vis spectroscopy (Figure 6A, Soret band at 420 nm, Q_α and Q_β bands at 565 and 540 nm, respectively). A similar spectrum is found for GLB-3b (not shown). CO ligation to the ferrous form is found to occur very slowly (Figure S15A-B, S16). The RR spectra of the CO-ligated form of ferrous GLB-3a were recorded at 1 mW (Figure 6B,C), and at 50 mW laser power (Figure S7). Already at 1 mW laser power photolysis occurs as is evident

by the observation of two ν_4 marker bands at 1373 cm^{-1} and ν_4 = 1362 cm^{-1}, agreeing with the CO-ligated and photolyzed ferrous form. At 50 mW laser power, full photolysis occurs (Figure S7B). Once the CO is photodissociated from the heme iron, the distal histidine will compete with the CO ligand to coordinate to the heme iron. The absence of a ν_3 contribution from a HS pentacoordinated (5c/HS) ferrous heme iron (around 1470 cm^{-1}) indicates fast recombination of the distal His.

The $\nu_{Fe–CO}$ stretching mode is dependent on the strength of the interaction of the CO ligand and the surrounding amino-acid residues. However, due to the very high fraction of photolysis at low laser power, accurate determination of this stretching mode is challenging even when studying the isotopic shift in the ^{13}CO adduct (Figure S8). The relative decrease of the 490 cm^{-1} signal when comparing the RR spectra with low and high laser power and the very weak signal at 487 cm^{-1} in the difference RR spectrum comparing ^{12}CO and ^{13}CO-ligated ferrous GLB-3a suggest that this is the $\nu_{Fe–CO}$ stretching mode. It can be ascribed to an open conformation of the heme pocket, with a weak interaction between CO and nearby amino acids [67]. However, it is important to note that this $\nu_{Fe–CO}$ signal is very weak and that the assignment remains ambiguous.

The strong competition with the distal His also follows from the CO-binding kinetics study (for details see Section S8, supplementary material). Flash photolysis of CO-ligated GLB-3a and GLB-3b (Figure S17) showed that the CO rebinding phase after the flash is very slow, since after 100 ms the difference in absorbance is still not zero. The stopped-flow measurements show that it takes around 300 seconds at the lowest CO concentration to replace the distal His (Figure S15A and B), which only requires 1 second for human Ngb [68]. To probe the role of the distal His, the CO-binding of the HE7A GLB-3 mutants were also measured with stopped flow. In contrast to the WT protein, only a few seconds are needed for the complete replacement of the distal ligand with CO (Figure S15C and D). While CO rebinding processes in globins can often be well modeled with a

biphasic model [23], the maximum entropy method (MEM) analysis shows for GLB-3 a much more complex CO recombination behavior (Figure S18). The very slow CO-binding due to the competition of the distal His and the high auto-oxidation rate seems to exclude a 'classic' gas binding function for GLB-3.

3.8 Potential enzymatic activity

Since binding of diatomic ligands seems not to be biologically relevant for GLB-3, the catalase activity, reaction with hydrogen sulfide and nitrite reductase activity of both WT GLB-3 isoforms, GLB-3a C70S and GLB-3 GD have been tested (Figures S20-S22). None of these proteins exhibited catalase activity after substrate addition (Figure S20). Moreover, ferric GLB-3a is very stable under extremely high H_2O_2 stress. GLB-3b, GLB-3a C70S and GLB-3 GD resist less to higher amounts of H_2O_2. The lack of extensions in GLB-3 GD leads in particular to a very unstable protein at high H_2O_2 concentrations (Figure S20D).

Some globins have been shown to be able to reduce H_2S to thiosulphate and hydropolysulphides [45, 69]. Addition of H_2S to the ferric wild-type GLB-3 isoforms and GLB-3a C70S induces no spectral change in contrast to the observations for human Ngb for which a slow reaction with H_2S is reported (Figure S21) [45]. Interestingly, incubation of ferric GLB-3 GD with H_2S for 50 minutes leads to the ferrous state (Figure S21D). This suggests that the protein extensions play an active role in hampering the reaction with H_2S.

In a third set of experiments, the nitrite reductase activity of the ferrous deoxy WT GLB-3, GLB-3a C70S and GLB-3 GD was tested (Figures S22). For this, the ferric globins were reduced with dithionite after which sodium nitrite was added. No nitrite reductase activity could be observed. In contrast, addition of nitrite to ferrous HE7A GLB-3a induces spectral changes in line with the

formation of an NO-ligated ferrous form. The nitrite reductase activity of HE7A GLB-3a shows that the E7His residue is key in hampering this activity in WT GLB-3.

3.9 Redox potential

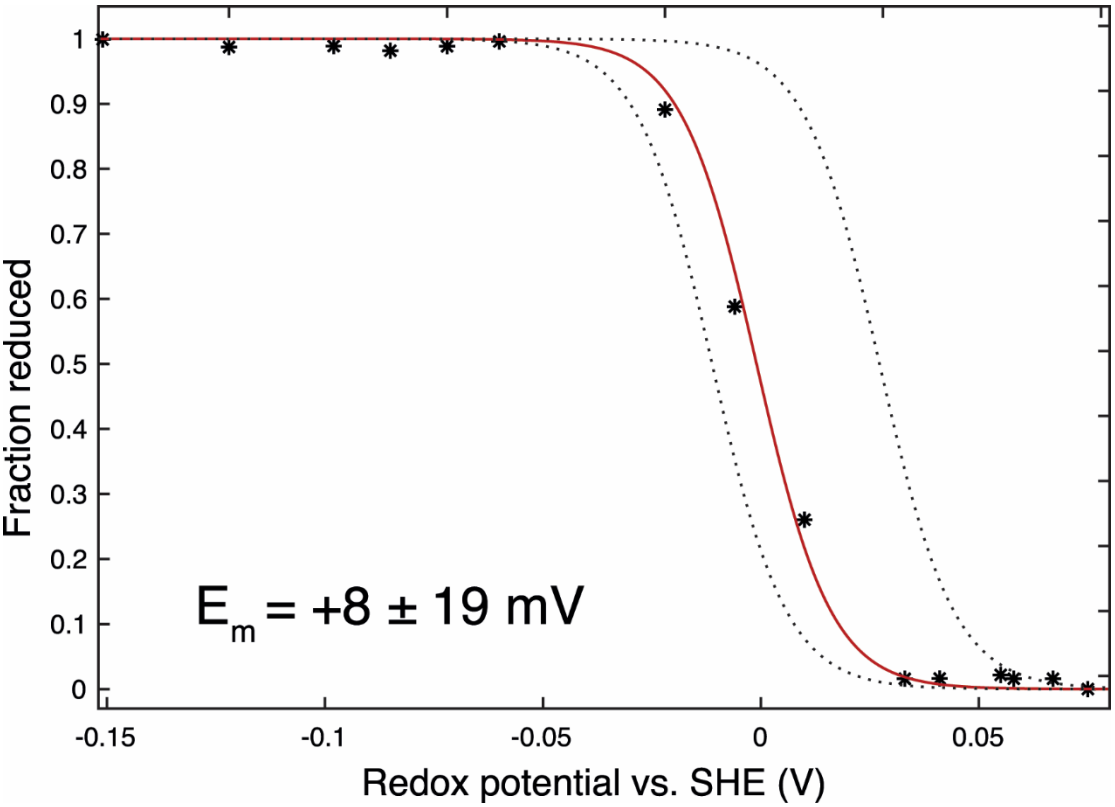

Figure 9. The plot shows the fit of the fraction reduced to the Nernst equation of one data set (solid red line). The measured E_m value is +8 ± 19 mV vs. SHE, which is an average of three experiments. The standard deviation is shown as dashed lines. The titrations were carried out at 25 °C in a mediator mix solution in 100 mM sodium phosphate buffer pH 7.

The redox potential of WT GLB-3a was measured via potentiometric redox titrations. The change in population from the Fe(III) to the Fe(II) state after each titration with dithionite was monitored through the spectral differences in the absorbance spectra at 530 and 560 nm, and double-checked using the changes in the Soret band (Figure S23). The fraction of reduced protein was normalized, plotted against the measured potential vs. SHE, and fitted to the Nernst equation (Figure 9). The

obtained redox potential E_m is +8 mV ± 19 mV vs. SHE, which falls within the wide range of E_m values reported for heme proteins (Table 3).

A peculiar feature was observed during the measurements: when approaching the midpoint potential E_m, addition of dithionite leads to the appearance of the spectrum of the reduced ferrous form, which then returned after several minutes to that of the oxidized species till an equilibrium was reached. Past the midpoint potential, the absorption spectra stayed those of the reduced ferrous state and did not change in time for a given potential. This observation may be linked to the fact that the proteins are cysteine rich.

Table 3. The redox potentials (Fe^{2+}/Fe^{3+} couple) of various heme proteins. The redox potential of GLB-3a compared with various hexa- and pentacoordinated heme proteins

Protein	E_m (mV) vs. SHE	Axial ligands	Ref.
Human cytochrome b_5	-21	His/His	[70]
Cytochrome c_3	-400	His/His	[71]
Cytochrome b_{559}	+395	His/His	[72]
Cytochrome c	+263	Met/His	[73]
Horseradish peroxidase	-250	His	[74]
Arabidopsis thaliana Hb1 and Hb2	-35	His/His	[75]
Arabidopsis thaliana Hb3	+15	His	[75]
Rice nsHb1	-143	His/His	[76]
Lumbricus Hb	+311	His	[77]
Human Mb	+50	His	[78]
Human Ngb* (mutated surface Cys)	-136	His/His	[79]
Human Ngb	-118	His/His	[80]
Human cytoglobin	-33	His/His	[81]
Kumaglobin	-400	His/His	[82]
C. elegans GLB-3a	+8	His/His	This work
C. elegans GLB-6	-193	His/His	[19]
C. elegans GLB-12	0	His/His	[11]
C. elegans GLB-26	+30	His/His	[21]

3.10 Unusual pH stability

Ferric GLB-3a exhibits an unusually high ability to bind heme at low pH values (Figure 10). No spectral changes are observed in the UV-Vis absorption spectra from pH 2 till 9.5 (with DTT) or pH 7.5 (without DTT). At pH 10.5 a small shift and decrease in the Soret band is detected in agreement with the alkaline transition to a hydroxide-ligated form. Figure 10 shows the comparison with ferric NGB and ferric horse heart myoglobin (hhMb). While the former has a 6c/LS heme coordination, the latter is in a hexacoordinated aquomet (6c/HS) form. An earlier report described the unusual stability of NGB at low pH in comparison to other globins [83]. Indeed, while aquomet hhMb has fully lost the heme group at pH 3.5, NGB releases its prosthetic group at a considerably slower rate at this pH (Figure 10). However, GLB-3a clearly surpasses this with the heme binding remaining intact even at pH 2. Interestingly, Hell's gate globin I, a globin from the acidophilic and thermophilic obligate ethanotroph *Methylacidiphilum infernorum* could be kept overnight at pH 2.8 when bound to acetate [84]. While at higher pH, no alkaline transition is found for ferric NGB, this does occur for GLB-3a. The addition of DTT seems to shift this transition to higher pH, whereby an effect of DTT on the pH is likely. The alkaline transition of ferric hhMb is known to occur at lower pH ~9 [85] as confirmed here (Figure 10). Moreover, the N- and C-terminal extensions of GLB-3 seem to have an effect on the heme region (Figure S24). Removal of these extensions decreases the heme-binding ability at lower pH and facilitates the hydroxide transition at less alkaline pH.

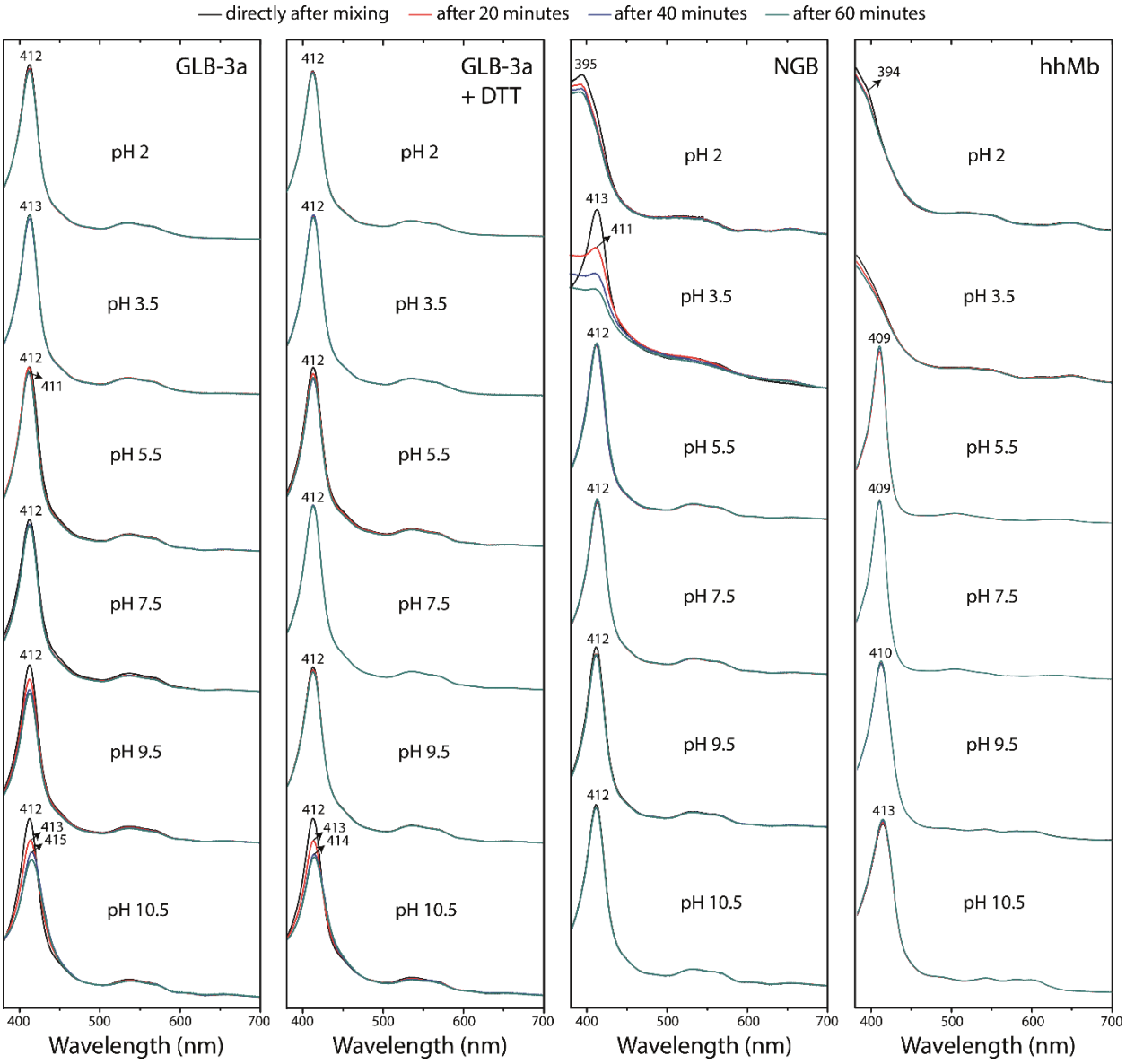

Figure 10. pH stability of ferric GLB-3a. UV-Vis absorption spectra of as-purified ferric GLB-3a, GLB-3a with DTT (similar for GLB-3b), and NGB and hhMb as control experiments, at different pH-values measured at different time points.

4. DISCUSSION

GLB-3a and GLB-3b are two isoforms of GLB-3 that contain a globin domain that is modelled to exhibit the classical 3/3 α-helical fold (Figure 8). The longest isoform, GLB-3b, is predicted to be

palmitoylated and myristoylated, while the smaller isoform is predicted to have a palmitoylation site and an additional N-terminal mitochondrial targeting site (MTS) (Figure S1C).

4.1. Heme pocket region

The heme iron is found to be bis-histidine coordinated (6c/LS) in both the ferric and ferrous form. EPR reveals that three LS forms (LS1-3) are present in ferric WT GLB-3, whereby LS3 disappears upon addition of DTT and is thus linked to disulphide-bridge formation. LS3 is not present in ferric GLB-3a C70S (Figure 7e), indicating Cys70 as one of the partners in the disulphide bridge. Homology modelling shows that Cys70 is buried in the protein matrix and can form an intramolecular disulphide bridge with Cys134 or Cys135. For human neuroglobin it has been shown that formation of an intramolecular disulphide bridge affects the heme pocket structure and influences the affinity to bind E7His [41,86]. Note that Cys134 and Cys135 are predicted as palmitoylation site and that the conditions for the formation of the intramolecular disulphide bridge may be different *in vivo*. Although MS shows that intermolecular disulphide bridges can be formed at the high protein concentrations used in EPR, this does not seem to be linked to LS3 formation. The occurrence of different LS forms indicates a flexibility in the heme region. The EPR parameters of bis-histidine coordinated heme centres can be linked to the relative orientation of the two imidazole planes of the iron-ligating E7His and F8His [41,87], with increasing g_z values indicating an increasing dihedral angle between the two imidazole planes and/or tilting of the imidazole plane away from the perpendicular position versus the heme plane. The g_z values found for LS1-3 (Table 2) agree with dihedral angles between the imidazole planes larger than 40^o [87]. LS3 has the largest g_z value revealing that formation of the disulphide bond exercises a strain on

the heme pocket. This may point to control of the GLB-3 function through the redox state of the disulphide bridge, as suggested for human neuroglobin [88].

Although the strong changes in the UV-Vis and EPR features of the GLB-3a HE7A variant compared to the WT form confirm the distal ligation of E7His to the heme iron in the latter form, an unexpected binding of an S-containing ligand, most likely Cys, to the heme iron is observed, suggesting that mutation of the distal His is accompanied by heme sliding or movement of the E-helix (nearest Cys on E2 and E12). This confirms the flexibility of the heme pocket and reveals that E7His plays a key stabilizing role in the protein structure, besides its role in the protein's function.

The CD spectra of all GLB-3 isoforms and variants show an unusual negative sign of the Soret CD band for the ferric forms, which seems independent of the distal heme ligand. Studies on Mb have shown that the sign and magnitude of the Soret CD band are strongly influenced by the interactions with the heme distal amino acids and the heme side chains (especially 2,4-vinyls and 6,7-propionates) [89,90]. The RR spectra of ferric GLB-3a indicate a strong hydrogen bonding of the propionate side chains with the protein matrix (Figure 6). Homology modelling reveals different hydrophobic and aromatic residues near the heme centre. Interactions of the heme plane with the aromatic residues is demonstrated to induce a negative sign of the Soret CD band [91].

4.2. C- and N-terminal extensions

The two isoforms of GLB-3 differ strongly in their N-terminal extension (Figure S1). *In vitro*, higher protein stability is observed for GLB-3a than for GLB-3b (Figure 3), most likely due to the smaller N-terminal extension of GLB-3a with less Cys residues and hence less oligomerization through intermolecular disulphide bonds. The longer N-terminal extension is likely responsible for the observed distribution of higher charge state ions in the MS analysis in GLB-3b (Figure 4B).

This extension is more flexible and not tightly packed to the protein core as shown via gel-filtration, and predicted to be unfolded, attracting more positive charges.

The presence of the C- and N-terminal extension has a clear influence on the GD. The GLB-3 GD variant is observed to be less stable under high excesses of H_2O_2 than GLB-3a and GLB-3b (Figure S20). Similarly, the absence of the C- and N-terminal parts reduces the heme-binding ability at very low pH (Figure 10 versus Figure S24). This indicates that the unexpected high stability of the heme binding is not merely due to the strong bis-histidine coordination of the heme iron and the hydrophobic heme pocket, but also linked to an extra stabilization/protection *via* the extensions.

Moreover, the C- and N-terminal extensions prevent the *in vitro* reaction with H_2S. A slow chemical reduction of ferric GLB-3 GD is observed in the presence of H_2S, while this is not occurring for the WT isoforms (Figure S21). Also the alkaline transition is somewhat affected by the removal of the extensions (Figure S24). This confirms the flexibility of the heme pocket area and the non-innocent effect of the extensions on the globin domain.

N-terminal extensions are also observed in many non-redundant globins [92], including other *C. elegans* globins [10], vertebrate Cygb [36] and globin X [15]. Although the functional relevance of the extensions is in many cases largely unclear, a majority of these globins carry myristoylation sites and/or palmitoylation sites, which led Blank and Burmester to the suggestion that respiratory globins may have evolved from a membrane-bound ancestor with signalling or lipid protective function [92], a hypothesis which has, however, not been substantiated since. The extensions of the GLB-3 isoforms may indeed function as signal sequences for subcellular location or membrane anchoring as found for *C. elegans* GLB-12 [11] and GLB-26 [21] (Table 1). Interestingly, Hanai *et al.* reported that the C-terminal extension of human cytoglobin is critical for the structural stability [93], in line with the observations for the extensions of GLB-3.

4.3. A cysteine-rich globin

An intriguing question is why the GLB-3 isoforms possess so many Cys residues. A high number of Cys residues in globins is found to be most common in nematode globins (Figure S2). Besides the well-known structural function of disulphide bonds and the earlier mentioned involvement in membrane linkage (palmitoylation sites), Cys residues are known to participate in different redox reactions. Redox-active Cys residues can play an important role in the regulation of the protein function as they may act as redox-sensing molecular switches which sense cellular oxidizing factors such as ROS and cellular reducing factors [94]. Additionally, like the redox-active Tyr and Trp residues, also Cys residues can act as intermediate charge carriers in electron transfer reactions as observed during the redox titration measurements [95]. A very recent chemoproteomics study determined the reactivity of the *C. elegans* cysteine proteome under physiological conditions [96]. Unfortunately, this study only picked up GLB-1 (with a non-redox active Cys), and revealed no information on the other 33 globins. Nevertheless, this study revealed wide-ranging redox regulation via cysteine redox chemistry in *C. elegans*, and showed redox-sensitive events in translation, growth signalling and stress response pathways. The high resistance of the heme-pocket region of GLB-3 to H_2O_2 may indicate that the cysteine-rich GLB-3 protein is designed to function in the presence of ROS. As a protecting mechanism, the globin thiols in nematodes can have a key role in thiol-mediated redox signalling in response to oxidative stress.

4.4. GLB-3 localization and potential function.

GLB-3 is expressed in the reproductive and nervous system. Mutation of *glb-3* leads to an almost complete loss of fertility. The absence of the *glb-3* gene also causes strong reduction of motility and pharyngeal pumping rate. The expression pattern of GLB-3 shows a strong resemblance to

that of GLB-12, which is also expressed in both neurons and the gonadal sheath [11]. However, there is no spatial overlap in the gonadal expression pattern of both globins, hinting at functional non-redundancy. While GLB-12 is reported to be expressed in the distal gonadal sheath, the proximal part of the spermatheca and the uterus, GLB-3 is observed in the proximal pair of gonadal sheath cells at the end of the oviduct, close to the spermatheca. Since these sheath cells are rich in muscle filaments, which help in the ovulation process, GLB-3 may regulate ovulation rate, possibly via redox signalling. Also, GLB-3 seems not to be present in neither HSN nor VC motoneurons, two main components in the egg-laying neuronal circuit [97]. Therefore, we can presume that knockout of GLB-3 expression in the gonadal sheet and not knockout of neuronal GLB-3 must be responsible for the fecundity defect.

Several *in vitro* observations, such as the slow binding of CO and the fast auto-oxidation, indicate that GLB-3 is not a transport/storage protein and is not involved in binding of diatomic (signalling) gases. A fast auto-oxidation hampering *in vitro* study of the oxy form of the globin was also observed in the *C. elegans* proteins GLB-6 [19], GLB-12 [11], and GLB-26 [21,16]. Even though the hydrophobic heme pocket of GLB-3 should prevent heme oxidation, polar amino-acid residues are observed at the entrance of the heme pocket (Figure 8). This is also the case for GLB-12, where the polar residues allow solvent access to the heme pocket and trigger heme iron oxidation [11].

A more likely function thus points towards a redox or electron-transfer function. *In vitro,* the GLB-3 forms showed no catalase activity nor nitrite reductase activity in contrast to many other globins. Oxidation of H_2S with concomitant reduction of the heme centre was only observed for the GLB-3 GD variant, hinting to protective influence of the N- and C-terminal extensions. The measured redox potential for GLB-3a is slightly positive (vs. SHE). For bis-histidyl ligated globins, a wide range of redox potentials is found presumably determining their function (Table 3). Such broad

range is also observed for cytochromes; even though the oxidation and reduction involve a seemingly simple reaction of electron transfer from or to the heme iron, their redox potentials span a range of several 100s of mV (Table 3). The redox potential is strongly influenced by the nature of the axial ligands to the heme iron, porphyrin peripheral substituents, solvent accessibility of the metal site, electrostatic interactions with protein side chains and other cofactors, and protonation state of neighboring amino-acid residues [98]. The E_m value of GLB-3a is higher than the reported redox potentials of the disulphide redox couples in human neuroglobin (-194 mV) [99] and human cytoglobin (-189 mV) [100], suggesting that the ferric heme iron of GLB-3a can oxidize disulphide bonds better than neuroglobin and cytoglobin.

The resilience of the protein and heme region to high concentrations of H_2O_2 and low pH indicate that the protein may be functional under harsh conditions, such as stress-induced ROS. *C. elegans* nematodes have H_2O_2 sensing neurons, which allow them to move away from hydrogen peroxide, that is produced by a wide variety of microorganisms and forms a lethal treat to the nematodes in their search for food [101]. Interestingly, GLB-3 is expressed in many of the neurons that were found to be essential in this response.

Further systematic biochemical studies are needed to identify potential redox partners or even a possible involvement in electron-transport or sensory function.

ABBREVIATIONS

C. elegans	*Caenorhabditis elegans*	RR	Resonance Raman
CD	Circular dichroism	S family	Sensor family
CT band	Charge-transfer band	SHE	Standard hydrogen electrode
CW EPR	Continuous-wave electron paramagnetic resonance	SwMb	Sperm whale myoglobin
GD	Globin domain	T family	Truncated family
Hb	Hemoglobin	WT	Wild type
hhMb	Horse heart myoglobin		
HS	High-spin		
IM-MS	Ion mobility-mass spectrometry		
LS	Low-spin		
M family	Myoglobin-like family		
Mb	Myoglobin		
MEM	Maximum entropy method		
MS	Mass spectrometry		
MTS	Mitochondrial targeting site		
MW	Molecular weight		
Ngb	Neuroglobin		
RNS	Reactive nitrogen species		
ROS	Reactive oxygen species		

AUTHOR INFORMATION

Zainab Hafideddine: Conceptualization, Methodology, Validation, Formal analysis, Visualization, Writing - Original Draft, Writing - Review & Editing

Tim Loier: Investigation, Formal analysis, Formal analysis, Visualization, Writing - Original Draft, Writing - Review & Editing

Niels Van Brempt: Validation, Formal analysis, Writing - Review & Editing

Sasha De Henau: Investigation, Resources, Writing - Review & Editing

H. Y. Vincent Ching: Investigation, Formal analysis, Writing - Review & Editing

Sander Neukermans: Investigation, Writing - Review & Editing

Saskia Defossé: Investigation, Writing - Review & Editing

Herald Berghmans: Investigation, Writing - Review & Editing

Roberta Sgammato: Investigation, Writing - Review & Editing

Roy Aerts: Investigation, Formal analysis, Visualization, Writing - Original Draft, Writing - Review & Editing

Dietmar Hammerschmid: Investigation, Formal analysis, Visualization, Writing - Original Draft, Writing - Review & Editing

Rani Moons: Investigation, Writing - Review & Editing

Tom Breugelmans: Supervision, Writing - Review & Editing

Frank Sobott: Supervision, Writing - Review & Editing, Funding acquisition

Christian Johannessen: Supervision, Writing - Review & Editing

Wouter Herrebout: Supervision, Writing - Review & Editing

Bart P. Braeckman: Supervision Writing - Original Draft, Funding acquisition

Luc Moens: Supervision, Writing - Review & Editing

Sylvia Dewilde: Conceptualization, Supervision, Funding acquisition

Sabine Van Doorslaer: Conceptualization, Methodology, Formal analysis, Supervision, Writing - Original Draft, Writing - Review & Editing, Funding acquisition

FUNDING

This work was supported by the Fund of Scientific Research-Flanders (FWO) (Grant number G0C3518N). The N2 Bristol strain was provided by the CGC, which is funded by NIH Office of Research Infrastructure Programs (P40 OD010440).

ACKNOWLEDGEMENTS

VC2879 was provided by the *C. elegans* Reverse Genetics Core Facility at the University of British Columbia, which is part of the international C. elegans Gene Knockout Consortium. We also thank Claudio D. Schuster from the University of Buenos Aires (FCEyN-UBA) for providing us the files of the globin database. Ina Devos is thanked for careful reading of the manuscript.

REFERENCES

1. S.N. Vinogradov, L. Moens, Diversity of globin function: Enzymatic, transport, storage, and sensing, J. Biol. Chem. 283 (2008) 8773–8777. https://doi.org/10.1074/jbc.R700029200.
2. D.A. Gell, Structure and function of haemoglobins, Blood Cells, Mol. Dis. 70 (2018) 13–42. https://doi.org/10.1016/j.bcmd.2017.10.006.
3. A.M. Lesk, J.T.J. Lecomte, The Globin Family, in: A. Bateman, C. Orengo (Eds.) Protein Families: Relating Protein Sequence, Structure, and Function, John Wiley & Sons, Inc., New Jersey, 2013, pp. 207-235. https://doi.org/10.1002/9781118743089.ch9.

4. A. Keppner, D. Maric, M. Correia, T.W. Koay, I.M.C. Orlando, S.N. Vinogradov, D. Hoogewijs, Lessons from the post-genomic era: Globin diversity beyond oxygen binding and transport, Redox Biol. 37 (2020) 101687. https://doi.org/10.1016/j.redox.2020.101687.
5. I.I. Vlasova, Peroxidase Activity of Human Hemoproteins: Keeping the Fire under Control, Molecules 23 (2018) 2561. https://doi.org/10.3390/molecules23102561.
6. B. Jensen, A. Fago, Reactions of ferric hemoglobin and myoglobin with hydrogen sulfide under physiological conditions, J. Inorg. Biochem. 182 (2018) 133–140. https://doi.org/10.1016/j.jinorgbio.2018.02.007.
7. D. Hoogewijs, E. Geuens, S. Dewilde, L. Moens, A. Vierstraete, S. Vinogradov, J.R. Vanfleteren, Genome-wide analysis of the globin gene family of C. elegans, IUBMB Life 56 (2004) 697–702. https://doi.org/10.1080/15216540500037562.
8. D. Hoogewijs, E. Geuens, S. Dewilde, A. Vierstraete, L. Moens, S. Vinogradov, J.R. Vanfleteren, Wide diversity in structure and expression profiles among members of the Caenorhabditis elegans globin protein family, BMC Genomics 8 (2008) 1–19. https://doi.org/10.1186/1471-2164-8-356.
9. D. Hoogewijs, S. De Henau, S. Dewilde, L. Moens, M. Couvreur, G. Borgonie, S.N. Vinogradov, S.W. Roy, J.R. Vanfleteren, The Caenorhabditis globin gene family reveals extensive nematode-specific radiation and diversification, BMC Evol. Biol. 8 (2008) 1–13. https://doi.org/10.1186/1471-2148-8-279.
10. L. Tilleman, F. Germani, S. De Henau, E. Geuens, D. Hoogewijs, B.P. Braeckman, J.R. Vanfleteren, L. Moens, S. Dewilde, Globins in Caenorhabditis elegans, IUBMB Life. 63 (2011) 166–174. https://doi.org/10.1002/iub.443.

11. S. De Henau, L. Tilleman, M. Vangheel, E. Luyckx, S. Trashin, M. Pauwels, F. Germani, C. Vlaeminck, J.R. Vanfleteren, W. Bert, A. Pesce, M. Nardini, M. Bolognesi, K. De Wael, L. Moens, S. Dewilde, B.P. Braeckman, A redox signalling globin is essential for reproduction in Caenorhabditis elegans, Nat. Commun. 6 (2015) 1–14. https://doi.org/10.1038/ncomms9782.
12. Ramandeep, K.W. Hwang, M. Raje, K.J. Kim, B.C. Stark, B. K.L. Dikshit, D.A. Webster, Vitreoscilla hemoglobin: Intracellular localization and binding to membranes, J. Biol. Chem. 276 (2001) 24781–24789. https://doi.org/10.1074/jbc.M009808200.
13. C. Liu, Y. He, Z. Chang, Truncated hemoglobin o of Mycobacterium tuberculosis: The oligomeric state change and the interaction with membrane components, Biochem. Biophys. Res. Commun. 316 (2004) 1163–1172. https://doi.org/10.1016/j.bbrc.2004.02.170.
14. B. Ertas, L. Kiger, M. Blank, M.C. Marden, T. Burmester, A membrane-bound hemoglobin from gills of the green shore crab Carcinus maenas, J. Biol. Chem. 286 (2011) 3185–3193. https://doi.org/10.1074/jbc.M110.160341.
15. M. Blank, J. Wollberg, F. Gerlach, K. Reimann, A. Roesner, T. Hankeln, A. Fago, R.E. Weber, T. Burmester, A membrane-bound vertebrate globin, PLoS One 6 (2011) e25292–e25292. https://doi.org/10.1371/journal.pone.0025292.
16. E. Geuens, D. Hoogewijs, M. Nardini, E. Vinck, A. Pesce, L. Kiger, A. Fago, L. Tilleman, S. De Henau, M.C. Marden, R.E. Weber, S. Van Doorslaer, J. Vanfleteren, L. Moens, M. Bolognesi, S. Dewilde, Globin-like proteins in Caenorhabditis elegans: in vivo localization, ligand binding and structural properties, BMC Biochem. 11 (2010) 17. https://doi.org/10.1186/1471-2091-11-17.

17. A. Persson, E. Gross, P. Laurent, K.E. Busch, H. Bretes, M. De Bono, Natural variation in a neural globin tunes oxygen sensing in wild Caenorhabditis elegans, *Nature* 458 (2009) 1030–1033. https://doi.org/10.1038/nature07820.
18. P.T. McGrath, M.V. Rockman, M. Zimmer, H. Jang, E.Z. Macosko, L. Kruglyak, C.I. Bargmann, Quantitative Mapping of a Digenic Behavioral Trait Implicates Globin Variation in C. elegans Sensory Behaviors, Neuron 61 (2009), 692–699. https://doi.org/10.1016/j.neuron.2009.02.012.
19. J. Yoon, M.A. Herzik, M.B. Winter, R. Tran, C. Olea, M.A. Marletta, Structure and properties of a bis-histidyl ligated globin from Caenorhabditis elegans, Biochemistry 49 (2010) 5662–5670. https://doi.org/10.1021/bi100710a.
20. C. Ren, Y. Li, R. Han, D. Gao, W. Li, J. Shi, D. Hoogewijs, B.P. Braeckman, S. De Henau, Y. Lu, W. Qu, Y. Gao, Y. Wu, Z. Li, H. Liu, Z. Wang, C. Zhang, GLB-13 is associated with oxidative stress resistance in caenorhabditis elegans, IUBMB Life 65 (2013) 423–434. https://doi.org/10.1002/iub.1132.
21. L. Tilleman, S. de Henau, M. Pauwels, N. Nagy, I. Pintelon, B.P. Braeckman, K. de Wael, S. van Doorslaer, D. Adriaensen, J.P. Timmermans, L. Moens, S. Dewilde, An N-Myristoylated Globin with a Redox-Sensing Function That Regulates the Defecation Cycle in Caenorhabditis elegans, PLoS One 7 (2012) 1–9. https://doi.org/10.1371/journal.pone.0048768.
22. L. Kiger, L. Tilleman, E. Geuens, D. Hoogewijs, C. Lechauve, L. Moens, S. Dewilde, M.C. Marden, Electron transfer function versus oxygen delivery: A comparative study for several hexacoordinated globins across the animal kingdom, PLoS One 6 (2011) 1–10. https://doi.org/10.1371/journal.pone.0020478.

23. L. Tilleman, F. Germani, S. De Henau, S., Helbo, F. Desmet, H. Berghmans, S. Van Doorslaer, D. Hoogewijs, L. Schoofs, B.P. Braeckman, L. Moens, A. Fago, S. Dewilde, A globin domain in a neuronal transmembrane receptor of Caenorhabditis elegans and Ascaris suum: Molecular modeling and functional properties, J. Biol. Chem. 290 (2015) 10336–10352. https://doi.org/10.1074/jbc.m114.576520.

24. S. Brenner, The genetics of Caenorhabditis elegans, Genetics 77 (1974) 71–94. https://doi.org/10.1093/genetics/77.1.71.

25. H. Cai, I. Dhondt, L. Vandemeulebroucke, C. Vlaeminck, M. Rasulova, B.P. Braeckman, Cbp-1 acts in gabaergic neurons to double life span in axenically cultured caenorhabditis elegans, J. Gerontol. A Biol. Sci. Med. Sci. 74 (2019) 1198–1205. https://doi.org/10.1093/gerona/glx206.

26. M. Porta-de-la-Riva, L. Fontrodona, A. Villanueva, J. Cerón, Basic Caenorhabditis elegans methods: Synchronization and observation, J. Vis. Exp. 64 (2012) 4019. https://doi.org/10.3791/4019.

27. O. Hobert, PCR fusion-based approach to create reporter Gene constructs for expression analysis in transgenic C. elegans, Biotechniques 32 (2002) 728–730. https://doi.org/10.2144/02324bm01.

28. D. Raizen, B.M. Song, N. Trojanowski, Y.J. You, (2012) Methods for measuring pharyngeal behaviors, in: The C. elegans Reasearch Community (ed.), WormBook, Pasadena, 2012. https://doi.org/10.1895/wormbook.1.154.1.

29. S. Stoll, A. Schweiger, EasySpin, a comprehensive software package for spectral simulation and analysis in EPR, J. Magn. Reson. 178 (2006) 42–55. https://doi.org/10.1016/j.jmr.2005.08.013.

30. J. Tejero, C.E. Sparacino-Watkins, V. Ragireddy, S. Frizzell, M.T. Gladwin, Exploring the mechanisms of the reductase activity of neuroglobin by site-directed mutagenesis of the heme distal pocket, Biochemistry 54 (2015) 722–733. https://doi.org/10.1021/bi501196k.
31. WormBase: Nematode Information Resource [online], glb (gene class) https://wormbase.org/resources/gene%5C_class/glb%5C#01--10
32. D. Bashford, C. Chothia, A. M. Lesk, Determinants of a protein fold. Unique features of the globin amino acid sequences. J. Mol Biol. 196 (1987) 199-216. https://doi.org/10.1016/0022-2836(87)90521-3
33. M.L. Edgley, D.L. Baillie, D. L. Riddle, A.M. Rose, Genetic balancers, in: The C. elegans Reasearch Community (ed.), WormBook, Pasadena, 2006. https://doi.org/10.1895/wormbook.1.89.1
34. S. Taylor, G. Santpere, M. Reilly, L. Glenwinkel, A. Poff, R. McWhirter, C. Xu, A. Weinreb, M. Basavaraju, S. Cook, A. Barrett, A. Abrams, B. Vidal, C. Cros, I. Rafi, N. Sestan, M. Hammarlund, O. Hobert, D. Miller, Expression profiling of the mature C. elegans nervous system by single-cell RNA-Sequencing, bioRxiv (2019) 737577. https://doi.org/10.1101/737577.
35. Y. Sugita, M. Nagai, Y. Yoneyama, Circular dichroism of hemoglobin in relation to the structure surrounding the heme, J. Biol. Chem. 246 (1971) 383–388. https://doi.org/10.1016/S0021-9258(18)62502-5.
36. C. Lechauve, C., Chauvierre, S. Dewilde, L. Moens, B.N. Green, M.C. Marden, C. Célier, L. Kiger, Cytoglobin conformations and disulphide bond formation, FEBS J. 277 (2010) 2696–2704. https://doi.org/10.1111/j.1742-4658.2010.07686.x.

37. S. Hu, K.M. Smith, T.G. Spiro, Assignment of protoheme Resonance Raman spectrum by heme labeling in myoglobin, J. Am. Chem. Soc. 118 (1996) 12638–12646. https://doi.org/10.1021/ja962239e.

38. S.S. Stavrov, The effect of iron displacement out of the porphyrin plane on the resonance Raman spectra of heme proteins and iron porphyrins, Biophys. J. 65 (1993) 1942–1950. https://doi.org/10.1016/S0006-3495(93)81265-7.

39. F.A. Walker, Magnetic spectroscopic (EPR, ESEEM, Mössbauer, MCD and NMR) studies of low-spin ferriheme centers and their corresponding heme proteins, Coord. Chem. Rev. 185–186 (1999) 471–534.

40. S.V. Nistor, E. Goovaerts, S. Van Doorslaer, S. Dewilde, L. Moens, EPR-spectroscopic evidence of a dominant His-Fe^{III}-His coordination in ferric neuroglobin, Chem. Phys. Lett. 361 (2002) 355–361. https://doi.org/10.1016/S0009-2614(02)00961-2.

41. E. Vinck, S. Van Doorslaer, S. Dewilde, L. Moens, Structural Change of the Heme Pocket Due to Disulphide Bridge Formation Is Significantly Larger for Neuroglobin than for Cytoglobin, J. Am. Chem. Soc. 126 (2004) 4516–4517. https://doi.org/10.1021/ja0383322.

42. R. Bois-Poltoratsky, A. Ehrenberg, Magnetic and Spectrophotometric Investigations of Cytochrome b5, Eur. J. Biochem. 2 (1967) 361–365.

43. T.K. Das, H.C. Lee, S.M.G. Duff, R.D. Hill, J. Peisach, D.L. Rousseau, B.A. Wittenberg, J.B. Wittenberg, The heme environment in barley hemoglobin, J. Biol. Chem. 274 (1999) 4207–4212. https://doi.org/10.1074/jbc.274.7.4207.

44. N. Ponomarenko, J. Niklas, P.R. Pokkuluri, O. Poluektov, D.M. Tiede, Electron Paramagnetic Resonance Characterization of the Triheme Cytochrome from Geobacter

sulfurreducens, Biochemistry 57 (2018) 1722–1732. https://doi.org/10.1021/acs.biochem.7b00917.

45. M. Ruetz, J. Kumutima, B.E. Lewis, M.R. Filipovic, N. Lehnert, T.L. Stemmler, R. Banerjee, A distal ligand mutes the interaction of hydrogen sulfide with human neuroglobin, J. Biol. Chem. 292 (2017) 6512–6528. https://doi.org/10.1074/jbc.M116.770370.
46. M.R. Cheesman, P.J. Little, B.C. Berks, Novel Heme Ligation in a c-type Cytochrome Involved in Thiosulfate Oxidation: EPR and MCD of SoxAX from Rhodovulum sulfidophilum, Biochemistry 40 (2001) 10562–10569. https://doi.org/10.1021/bi0100081.
47. P.M.A. Gadsby, A.J. Thomson, Assignment of the axial ligands of ferric ion in low-spin hemoproteins by near-infrared magnetic circular dichroism and electron paramagnetic resonance spectroscopy, J. Am. Chem. Soc. 112 (1990) 5003–5011. https://doi.org/10.1021/ja00169a002.
48. A. Waterhouse, M. Bertoni, S. Bienert, G. Studer, G. Tauriello, R. Gumienny, F.T. Heer, T.A.P. De Beer, C. Rempfer, L. Bordoli, R. Lepore, T. Schwede, SWISS-MODEL: Homology modelling of protein structures and complexes, Nucleic Acids Res. 46 (2018) W296–W303. https://doi.org/10.1093/nar/gky427.
49. S. Bienert, A. Waterhouse, T.A.P. De Beer, G. Tauriello, G. Studer, L. Bordoli, T. Schwede, The SWISS-MODEL Repository-new features and functionality, Nucleic Acids Res. 45 (2017) D313–D319. https://doi.org/10.1093/nar/gkw1132.
50. N. Guex, M.C. Peitsch, T. Schwede, Automated comparative protein structure modeling with SWISS-MODEL and Swiss-PdbViewer: A historical perspective, Electrophoresis 30 (2009) S162-173. https://doi.org/10.1002/elps.200900140.

51. P. Benkert, M. Biasini, T. Schwede, Toward the estimation of the absolute quality of individual protein structure models, Bioinformatics 27 (2011), 343–350. https://doi.org/10.1093/bioinformatics/btq662.

52. M. Bertoni, F. Kiefer, M. Biasini, L. Bordoli, T. Schwede, T. Modeling protein quaternary structure of homo- and hetero-oligomers beyond binary interactions by homology, Sci. Rep. 7 (2017) 10480. https://doi.org/10.1038/s41598-017-09654-8.

53. A. Pesce, S. Dewilde, M. Nardini, L. Moens, P. Ascenzi, T. Hankeln, T. Burmester, M. Bolognesi, Human brain neuroglobin structure reveals a dinstinct mode of controlling oxygen affinity, Structure 11 (2003) 1087-1095. https://doi.org/10.1016/s0969-2126(03)00166-7.

54. L.A. Kelley, S. Mezulis, C.M. Yates, M.N. Wass, M.J.E. Sternberg, The Phyre2 web portal for protein modeling, prediction and analysis, Nat. Protoc. 10 (2015) 845–858. https://doi.org/10.1038/nprot.2015.053.

55. U. Pieper, B.M. Webb, D.T. Barkan, D. Schneidman-Duhovny, A. Schlessinger, H. Braberg, Z. Yang, E.C. Meng, E.F. Pettersen, C.C. Huang, R.S. Datta, P. Sampathkumar, M.S. Madhusudhan, K. Sjölander, T.E. Ferrin, S.K. Burley, A. Sali, ModBase, a database of annotated comparative protein structure models, and associated resources, Nucleic Acids Res. 39 (2011) D465-74. http://doi.org/10.1093/nar/gkq1091.

56. J.U. Bowie, R. Lüthy, D. Eisenberg, A method to identify protein sequences that fold into a known three-dimensional stucture, Science **253** (1991) 164–170. https://doi.org/10.1126/science.1853201.

57. R. Lüthy, J.U. Bowie, D. Eisenberg, Assessment of protein models with three-dimensional profiles, Nature 356 (1992) 83–85. https://doi.org/10.1038/356083a0.

58. M. Wiederstein, M.J. Sippl, ProSA-web: Interactive web service for the recognition of errors in three-dimensional structures of proteins, Nucleic Acids Res. 35 (2007) W407-10. https://doi.org/10.1093/nar/gkm290.

59. M.J. Sippl, Recognition of errors in three-dimensional structures of proteins, *Proteins* 17 (1993) 355–362. https://doi.org/10.1002/prot.340170404.

60. R.A. Laskowski, M.W. MacArthur, D.S. Moss, J.M. Thornton, PROCHECK: a program to check the stereochemical quality of protein structures, J. Appl. Crystallogr. 26 (1993) 283–291. https://doi.org/10.1107/S0021889892009944.

61. R.A. Laskowski, J.A.C. Rullmann, M.W. MacArthur, R. Kaptein, J.M. Thornton, AQUA and PROCHECK-NMR: Programs for checking the quality of protein structures solved by NMR, J. Biomol. NMR. 8 (1996) 477–486. https://doi.org/10.1007/BF00228148.

62. A. Drozdetskiy, C. Cole, J. Procter, G.J. Barton, JPred4: A protein secondary structure prediction server, Nucleic Acids Res. 43 (2015) W389–W394. https://doi.org/10.1093/nar/gkv332.

63. J. Jumper, R. Evans, A. Pritzel, T. Green, M. Figurnov, O. Ronneberger, K. Tunyasuvunakool, R. Bates, A. Žídek, A. Potapenko, A. Bridgland, C. Meyer, S. A. A. Kohl, A. J. Ballard, A. Cowie, B. Romera-Paredes, S. Nikolov, R. Jain, J. Adler, T. Back, S. Petersen, D. Reiman, E. Clancy, M. Zielinski, M. Steinegger, M. Pacholska, T. Berghammer, S. Bodenstein, D. Silver, O. Vinyals, A. W. Senior, K. Kavukcuoglu, P. Kohli, D. Hassabis, Highly accurate protein structure prediction with AlphaFold, Nature 596 (2021) 583-589. https://doi.org/10.1038/s41586-021-03819-2

64. M. Varadi, S. Anyango, M. Deshpande, S. Nair, C. Natassia, G. Yordanova, D. Yuan, O. Stroe, G. Wood, A. Laydon, A. Žídek, T. Green, K. Tunyasuvunakool, S. Petersen, J.

Jumper, E. Clancy, R. Green, A. Vora, M. Lutfi, M. Figurnov, A. Cowie, N. Hobbs, P. Kohli, G. Keywegt, E. Birney, D. Hassabis, AlphaFold Protein Strucutre Database: massively expanding the structural coverage of protein-sequence space with high-accuracy models. Nucleic Acids Research, 50 (2022) D439-D444, https://doi.org/10.1093/nar/gkab1061

65. E.F. Pettersen, T.D. Goddard, C.C. Huang, G.S. Couch, D.M. Greenblatt, E.C. Meng, T.E. Ferrin, UCSF Chimera - A visualization system for exploratory research and analysis, J. Comput. Chem. 25 (2004) 1605–1612. https://doi.org/10.1002/jcc.20084.
66. C.J.A. Wallace, I. Clark-Lewis, Functional role of heme ligation in cytochrome c. Effects of replacement of methionine 80 with natural and non-natural residues by semisynthesis, J. Biol. Chem. 267 (1992) 3852–3861. https://doi.org/10.1016/S0021-9258(19)50604-4.
67. T.G. Spiro, I.H. Wasbotten, CO as a vibrational probe of heme protein active sites, J. Inorg. Biochem.. 99 (2005) 34–44. https://doi.org/10.1016/j.jinorgbio.2004.09.026.
68. S. Dewilde, L. Kiger, T. Burmester, T. Hankeln, V. Baudin-Creuza, T. Aerts, M.C. Marden, R. Caubergs, L. Moens, Biochemical Characterization and Ligand Binding Properties of Neuroglobin, a Novel Member of the Globin Family, J. Biol. Chem. 276 (2001) 38949–38955. https://doi.org/10.1074/jbc.m106438200.
69. T. Bostelaar, V. Vitvitsky, J. Kumutima, B.E. Lewis, P.K. Yadav, T.C. Brunold, M. Filipovic, N. Lehnert, T.L. Stemmler, R. Banerjee, Hydrogen Sulfide Oxidation by Myoglobin, J. Am. Chem. Soc. 138 (2016) 8476-8488. https://doi.org/10.1021/jacs.6b03456.
70. T. Aono, Y. Sakamoto, M. Miura, F. Takeuchi, H. Hori, M. Tsubaki, Direct electrochemical analyses of human cytochromes b5 with a mutated heme pocket showed

a good correlation between their midpoint and half wave potentials, J. Biomed. Sci. 17 (2010) 90. https://doi.org/10.1186/1423-0127-17-90.

71. J.M. Shifman, B.R. Gibney, R.E. Sharp, P.L. Dutton, Heme Redox Potential Control in de Novo Designed Four-α-Helix Bundle Proteins, Biochemistry 39 (2000) 14813–14821. https://doi.org/10.1021/bi000927b.
72. P. Horton, J. Whitmarsh, W.A. Cramer, On the specific site of action of 3-(3,4-dichlorophenyl)-1,1-dimethylurea in chloroplasts: Inhibition of a dark acid-induced decrease in midpoint potential of cytochrome b-559, Arch. Biochem. Biophys. 176 (1976) 519–524. https://doi.org/10.1016/0003-9861(76)90195-8.
73. G. Battistuzzi, M. Borsari, J.A. Cowan, A. Ranieri, M. Sola, Control of cytochrome c redox potential: Axial ligation and protein environment effects, J. Am. Chem. Soc. 124 (2002) 5315–5324. https://doi.org/10.1021/ja017479v.
74. H. Yamada, R. Makino, I. Yamazaki, Effects of 2,4-substituents of deuteroheme upon redox potentials of horseradish peroxidases, Arch. Biochem. Biophys. 169 (1975) 344–353. https://doi.org/10.1016/0003-9861(75)90350-1.
75. A.C. Mot, C. Puscas, P. Miclea, G. Naumova-Letia, S. Dorneanu, D. Podar, N. Dissmeyer, R. Silaghi-Dumitrescu, Redox control and autoxidation of class 1, 2 and 3 phytoglobins from Arabidopsis thaliana, Sci. Rep. **8** (2018) 13714. https://doi.org/10.1038/s41598-018-31922-4.
76. S. Kakar, F.G. Hoffman, J.F. Storz, M. Fabian, M.S. Hargrove, Structure and reactivity of hexacoordinate hemoglobins, Biophys. Chem. 152 (2010) 1–14. https://doi.org/10.1016/j.bpc.2010.08.008.
77. S.C. Dorman, C.F. Kenny, L. Miller, R.E. Hirsch, J.P. Harrington, Role of redox potential

of hemoglobin-based oxygen carriers on methemoglobin reduction by plasma components, Artif. Cells. Blood Substit. Immobil. Biotechnol. 30 (2002) 39–51. https://doi.org/10.1081/bio-120002726.

78. S. ichi Adachi, S. Nagano, Y. Watanabe, K. Ishimori, I. Morishima, Alteration of human myoglobin proximal histidine to cysteine or tyrosine by site-directed mutagenesis: Characterization and their catalytic activities, Biochem. Biophys. Res. Commun. 180 (1991) 138–144. https://doi.org/10.1016/s0006-291x(05)81266-5.
79. S. Trashin, M. De Jong, E. Luyckx, S. Dewilde, K. De Wael, Electrochemical evidence for neuroglobin activity on NO at physiological concentrations, J. Biol. Chem. 291 (2016) 18959–18966. https://doi.org/10.1074/jbc.m116.730176.
80. J. Tejero, C.E. Sparacino-Watkins, V. Ragireddy, S. Frizzell, M.T. Gladwin, Exploring the mechanisms of the reductase activity of neuroglobin by site-directed mutagenesis of the heme distal pocket, Biochemistry 54 (2015) 722–733. https://doi.org/10.1021/bi501196k.
81. B. Cuypers, S. Vermeylen, D. Hammerschmid, S. Trashin, V. Rahemi, A. Konijnenberg, A. De Schutter, C.H.C. Cheng, D. Giordano, C. Verde, K. De Wael, F. Sobott, S. Dewilde, S. Van Doorslaer, Antarctic fish versus human cytoglobins – The same but yet so different, J. Inorg. Biochem. 173 (2017) 66–78. https://doi.org/10.1016/j.jinorgbio.2017.04.025.
82. K. Kobayashi, J. Kim, Y. Fukuda, T. Kozawa, T. Inoue, Fast autooxidation of a bis-histidyl-ligated globin from the anhydrobiotic tardigrade, Ramazzottius varieornatus, by molecular oxygen, J. Biochem. 169 (2021) 663-673. https://doi.org/10.1093/jb/mvab003.
83. P. Picotti, S. Dewilde, A. Fago, C. Hundahl, V. De Filippis, L. Moens, A. Fontana,

Unusual stability of human neuroglobin at low pH - Molecular mechanisms and biological significance, FEBS J. 276 (2009) 7027–7039. https://doi.org/10.1111/j.1742-4658.2009.07416.x.

84. A.H. Teh, J.A. Saito, A. Baharuddin, J.R. Tuckerman, J.S. Newhouse, M. Kanbe, E.I. Newhouse, R.A. Rahim, F. Favier, C. Didierjean, E.H.S. Sousa, M.B. Stott, P.F. Dunfield, G. Gonzalez, M.A. Gilles-Gonzalez, N. Najimudin, M. Alam, Hell's Gate globin I: An acid and thermostable bacterial hemoglobin resembling mammalian neuroglobin, FEBS Lett. 585 (2011) 3250–3258. https://doi.org/10.1016/j.febslet.2011.09.002.
85. G. Acampora, J. Hermans, Reversible Denaturation of Sperm Whale Myoglobin. I. Dependence on Temperature, pH, and Composition, J. Am. Chem. Soc. 89 (1967) 1543–1547. https://doi.org/10.1021/ja00983a001.
86. D. Hamdane, L. Kiger, S. Dewilde, B.N. Green, A. Pesce, J. Uzan, T. Burmester, T. Hankeln, M. Bolognesi, L. Moens, M.C. Marden, The Redox State of the Cell Regulates the Ligand Binding Affinity of Human Neuroglobin and Cytoglobin. J. Biol. Chem. 278 (2003) 51713–51721. https://doi.org/10.1074/jbc.m309396200.
87. F.A. Walker, The heme environment of mouse neuroglobin: histidine imidazole plane orientations obtained from solution NMR and EPR spectroscopy as compared with X-ray crystallography, J. Biol. Inorg. Chem. 11 (2006) 391-397. https://doi.org/10.1007/s00775-006-0095-8.
88. A.N. Morozov, J.P. Roach, M. Kotzer, D.C. Chatfield, A possible mechanism for redox control of human neuroglobin activity, J. Chem. Inf. Model. 54 (2014) 1997–2003. https://doi.org/10.1021/ci5002108.

89. M. Nagai, Y. Nagai, K. Imai, S. Neya, Circular dichroism of hemoglobin and myoglobin, Chirality **26** (2014) 438–442. https://doi.org/10.1002/chir.22273.

90. M. Nagai, C. Kobayashi, Y. Nagai, K. Imai, N. Mizusawa, H. Sakurai, S. Neya, M. Kayanuma, M. Shoji, S. Nagatomo, Involvement of propionate side chains of the heme in circular dichroism of myoglobin: Experimental and theoretical analyses, J. Phys. Chem. B. 119 (2015) 1275–1287. https://doi.org/10.1021/jp5086203.

91. A. Boffi, J.B. Wittenberg, E. Chiancone, Circular dichroism spectroscopy of Lucina I hemoglobin, FEBS Lett. 411 (1997) 335–338. https://doi.org/10.1016/s0014-5793(97)00727-8.

92. M. Blank, T. Burmester, Widespread Occurrence of N-terminal Acylation in Animal Globins and Possible Origin of Respiratory Globins from a Membrane-bound Ancestor, Mol. Biol. Evol. 29 (2012) 3553-3561. https://doi.org/10.1093/molbev/mss164.

93. S. Hanai, H. Tsujino, T. Yamashita, R. Torii, H. Sawai, Y. Shiro, K. Oohora, T. Hayashi, T. Uno, Roles of N- and C-terminal domains in the ligand-binding properties of cytoglobin, J. Inorg. Biochem. 179 (2018) 1–9. https://doi.org/10.1016/j.jinorgbio.2017.11.003.

94. N. Nagahara, Intermolecular disulfide bond to modulate protein function as a redox-sensing switch, Amino Acids 41 (2011) 59–72. https://doi.org/10.1007/s00726-010-0508-4.

95. M. Wang, J. Gao, P. Müller, B. Giese, Electron transfer in peptides with cysteine and methionine as relay amino acids, Angew. Chemie - Int. Ed. 48 (2009) 4232–4234. https://doi.org/10.1002/anie.200900827.

96. J. Meng, L. Fu, K. Liu, C. Tian, Z. Wu, Y. Jung, R.B. Ferreira, K.S. Carroll, T.K.

Blackwell, J. Yang, Global profiling of distinct cysteine redox forms reveals wide-ranging redox regulation in C. elegans, Nature Commun. 12 (2021) 1415. https://doi.org/10.1038/s41467-021-21686-3.

97. J.G. White, E. Southgate, J.N. Thomson, S. Brenner, The structure of the nervous system of the nematode Caenorhabditis elegans, Phil. Trans. R. Soc. Lond. B 314 (1986) 1–340. https://doi.org/10.1098/rstb.1986.0056.

98. J.M. Shifman, B.R. Gibney, R.E. Sharp, P.L. Dutton, Heme Redox Potential Control in de Novo Designed Four-α-Helix Bundle Proteins, Biochemistry 39 (2000) 14813–14821. https://doi.org/10.1021/bi000927b.

99. M. Tiso, J. Tejero, S. Basu, I. Azarov, X. Wang, V. Simplaceanu, S. Frizzell, T. Jayaraman, L. Geary, C. Shapiro, C. Ho, S. Shiva, D.B. Kim-Shapiro, M.T. Gladwin, Human neuroglobin functions as a redox-regulated nitrite reductase, J. Biol. Chem. 286 (2011) 18277–18289. https://doi.org/10.1074/jbc.M110.159541.

100. A.W. DeMartino, M.B. Amdahl, K. Bocian, J.J. Rose, J. Tejero, M.T. Gladwin, Redox sensor properties of human cytoglobin allosterically regulate heme pocket reactivity, Free Radic. Biol. Med. 162 (2021) 423–434. https://doi.org/10.1016/j.freeradbiomed.2020.10.321.

101. J.A. Schiffer, S.V. Sumbur, M. Seyedolmohadesin, Y. Xu, W.T. Serkin, N.G. McGowan, O. Banjo, M. Torkashvand, A. Lin, C.N. Hosea, C. N., A. Assié, B.S. Samuel, M.P. O'Donnell, V. Venkatachalam, J. Apfeld, Modulation of sensory perception by hydrogen peroxide enable Caenorhabditis elegans to find a nice that provide both food an protection from hydrogen peroxide, *PLOS Pathogens*, **17** (2021) e1010112. https://doi.org/10.1371/journal.ppat.1010112.